

Tunable giant Purcell enhancement of quantum light emitters by means of acoustic graphene plasmons

Justin Gruber,^{1,2} Mahtab A. Khan,^{3,4} Dirk R. Englund,⁵ and Michael N. Leuenberger⁶

¹⁾*College of Optics and Photonics (CREOL), University of Central Florida, Orlando, FL 32826, USA*

²⁾*The Institute of Optics, University of Rochester, Rochester, NY 14627, USA*

³⁾*NanoScience Technology Center, University of Central Florida, Orlando, FL 32826, USA.*

⁴⁾*Department of Physics, Federal Urdu University of Arts, Sciences and Technology, Islamabad, Pakistan.*

⁵⁾*Department of Electrical Engineering and Computer Science, Massachusetts Institute of Technology, Cambridge, MA 02139, USA*

⁶⁾*NanoScience Technology Center, Department of Physics, College of Optics and Photonics, University of Central Florida, Orlando, FL 32826, USA.^{a)}*

Inspired by the remarkable ability of plasmons to boost radiative emission rates, we propose leveraging acoustic graphene plasmons (AGPs) to realize tunable, giant Purcell enhancements for single-photon, entangled-photon, and multipolar quantum emitters. These AGPs are localized inside a cavity defined by a graphene sheet and a metallic nanocube and filled with a dielectric of thickness of a few nanometers and consisting of stacked layers of 2D materials, containing impurities or defects that act as quantum light emitters. Through finite-difference time domain (FDTD) calculations, we show that this geometry can achieve giant Purcell enhancement factors over a large portion of the infrared (IR) spectrum, up to 6 orders of magnitude in the mid-IR and up to 4 orders of magnitude at telecommunications wavelengths, reaching quantum efficiencies of 95% and 89%, respectively, with high-mobility graphene. We obtain Purcell enhancement factors for single-photon electric dipole (E1), electric quadrupole (E2), and electric octupole (E3) transitions and two-photon spontaneous emission (2PSE) transitions, of the orders of 10^4 , 10^7 , 10^9 , and 10^9 , respectively, and a quantum efficiency of 79% for entangled-photon emission with high-mobility graphene at a wavelength of $\lambda = 1.55 \mu\text{m}$. Importantly, AGP mode frequencies depend on the graphene Fermi energy, which can be tuned via electrostatic gating to modulate fluorescence enhancement in real time. As an example, we consider the Purcell enhancement of spontaneous single- and two-photon emissions from an erbium atom inside single-layer (SL) WS₂. Our results could be useful for electrically tunable quantum emitter devices with applications in quantum communication and quantum information processing.

Keywords: acoustic graphene plasmons, Purcell enhancement, rare-earth atoms, transition metal dichalcogenides, 2D materials

Single-photon emitters (SPEs) are a crucial technology in the development of quantum information technologies, and several methods for creating solid-state SPEs have been put forth.¹ Methods for creating SPEs include semiconductor quantum dots² and color centers caused by defects such as nitrogen-vacancy centers in diamond.³ An emerging class of SPEs are defect states in two-dimensional (2D) materials. Single photon emission has been demonstrated experimentally in a variety of 2D materials including hexagonal boron nitride (hBN),⁴ transition metal dichalcogenides (TMDs),^{5–10} and GaSe.¹¹

Silicon has recently emerged as a promising host for telecom-band single-photon sources based on color centers, compatible with foundry-scale photonics. First isolations of individual carbon-related G centers in silicon-on-insulator (SOI) established bright, linearly polarized emission near $1.28 \mu\text{m}$,¹² followed by surveys revealing multiple defect families and near-infrared single-photon emission¹³ and by wafer-scale, position-controlled creation of single G and W centers.¹⁴ Foundational studies clarified photophysics and lo-

calization effects¹⁵ and the subtle distinction between genuine and faux single G centers in carbon-implanted Si,¹⁶ while measurements resolved fine-structure and dipole characteristics of individual G centers in SOI structures.¹⁷ On the device side, Englund's group demonstrated individually addressable, waveguide-coupled G centers with spectral trimming on SOI photonic integrated circuits;¹⁸ extended this to tunable, foundry-scale circuits;¹⁹ and together with collaborators showed indistinguishable photon generation from a silicon artificial atom directly in silicon photonics.²⁰ Complementing this, the Kante/Qarony collaboration reported the first all-silicon atom–cavity source by embedding a single G center in a silicon photonic-crystal cavity, achieving strong Purcell acceleration and near-unity coupling efficiency.²¹ For the T center—a carbon–hydrogen complex attractive for spin–photon interfacing—high-efficiency single-photon emission was realized using a nanobeam geometry,²² and cavity-QED coupling of single T centers has now been demonstrated, with rate enhancement and improved zero-phonon-line (ZPL) extraction.^{23,24} In parallel, the Reiserer group established cavity-enhanced single-photon emission in silicon using nanophotonic resonators (including spin-resolved spectroscopy and Purcell factors of 78)²⁵ and later achieved cavity-enhanced single artificial atoms at telecom-

^{a)}Electronic mail: michael.leuenberger@ucf.edu

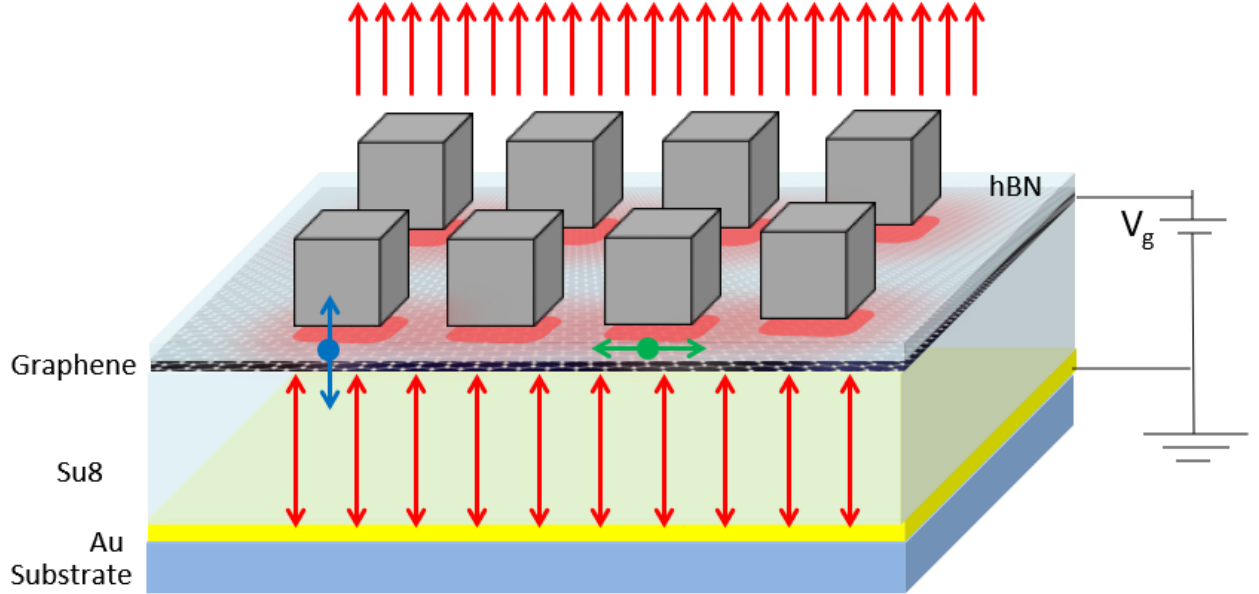


FIG. 1. Schematic of proposed AGP cavity and heterostructure. Dipole emitter is located within the hBN layer, with the perpendicular orientation shown in blue and the parallel orientation shown in green. The acoustic graphene plasmons (AGPs) are localized in the region between the nanocubes and the graphene layer(s).

munications wavelengths.²⁶ Together, these advances mark rapid progress from discovery to engineering: deterministic, CMOS-compatible placement,¹⁴ active spectral control and indistinguishability on-chip,^{18–20} and cavity integration across both G and T centers.^{21,23–26}

Er^{3+} centers provide quantum emission directly in the low-loss telecom C-band, making them natural building blocks for fiber-connected quantum networks. In silicon nanophotonics, narrow optical transitions²⁷ and strong Purcell enhancement in nanobeam cavities²⁵ have enabled cavity-coupled single-ion interfaces with optical single-shot spin readout²⁸ and long optical/spin coherence in isotopically enriched ^{28}Si .²⁹ These advances build on the earliest single-ion addressing of Er in Si³⁰ and recent demonstrations of reliable foundry integration of Er in low-loss silicon waveguides.³¹ Beyond Si, Awschalom and co-workers established a CMOS-compatible thin-film platform based on Er:TiO₂ on silicon, showing large Purcell factors and on-chip integration,³² followed by direct isolation of individual Er emitters in TiO₂ films³³ and systematic optical/microstructural studies.³⁴ In non-silicon crystals engineered for low spectral diffusion, indistinguishable single photons from a single Er^{3+} in CaWO_4 coupled to silicon nanophotonics have been observed with high Hong–Ou–Mandel visibility,³⁵ and spin–photon entanglement from a single Er ion has been reported.³⁶ Additional control knobs include electro-optic tuning and emission-rate control of single Er in thin-film LiNbO₃ photonic crystal cavities,^{37,38} and Stark tuning of single Er in Y_2SiO_5 by on-chip electrodes.³⁹ Together, these results map a clear route from discovery to engineering: telecom-band single photons

and spin–photon interfaces in silicon,^{25,27–29,31} scalable thin-film TiO₂ photonics,^{32–34} and host crystals tailored for indistinguishability and entanglement.^{35,36,39}

Two-dimensional (2D) semiconductors and insulators have rapidly emerged as versatile platforms for on-chip quantum light sources. In TMDs, spatially localized excitons in monolayer WSe₂ were the first 2D SPEs demonstrated in 2015, showing antibunched emission from defect/strain-localized states and inaugurating the field of quantum light in van der Waals materials.^{5–9} Since then, deterministic nano-/micro-strain engineering has enabled spatially ordered arrays of TMD SPEs and controlled polarization selection rules,^{40,41} while plasmonic and dielectric nanocavities have provided Purcell enhancement and improved out-coupling for integrated photonics.^{42,43} Beyond optical pumping, electrically driven devices based on WSe₂ tunneling junctions now realize site-controlled and even array-level single-photon electroluminescence.^{43–45}

A second major platform is hexagonal boron nitride (hBN), whose deep-level point defects host bright and photostable SPEs that operate at room temperature across visible to ultraviolet wavelengths.^{46–56} Considerable progress has been made in understanding spectral inhomogeneity, strain and Stark tuning, and in the near-deterministic activation/placement of emitters compatible with wafer-level processing and photonic integration.^{50,51,55–59} Together with robust room-temperature operation, these advances position hBN as a leading candidate for scalable quantum photonic circuits.

Recently, moiré superlattices in twisted TMD heterobilayers introduced a third route to single-photon emission via

moiré-trapped interlayer excitons (IXs). These emitters exhibit discrete, highly tunable lines, long lifetimes, and access to spin/valley physics, and they have been interfaced with high-*Q* nanocavities.^{60–66} Beyond fundamental interest, moiré IXs offer device-level knobs (twist angle, reconstruction, gating) that complement strain/defect control in monolayers.⁶⁷

Across all 2D platforms, the state-of-the-art has moved from proof-of-concept to engineering: room-temperature operation (hBN), deterministic positioning (strain-patterned TMDs and processed hBN), electrical injection (WSe₂ diodes), polarization/valley control, and cavity integration for enhanced brightness and indistinguishability.^{43,54,68} Remaining challenges include identifying and stabilizing microscopic defect configurations (hBN), mitigating spectral diffusion and dephasing, achieving narrow linewidths and high photon indistinguishability, and unifying electrical control with large-scale, CMOS-compatible integration.^{53,54,57,59}

Additionally, telecommunications makes extensive use of light at wavelengths near 1550 nm for transmission in fiber optics with minimum losses.^{69,70} For this reason, it has been of great interest to extend the emission range of SPEs to include 1550 nm. This has been achieved through the doping of TMDs, such as MoS₂ and WSe₂ with erbium (Er) ions.^{71,72} Alternatively, the engineering of defects in hBN has been proposed as a potential SPE near 1550 nm.⁷³

In order to improve the performance of an SPE, it can be placed inside an optical cavity, which increases the emission rate Γ of the SPE. If we take Γ_0 to be the emission rate in vacuum and Γ_{dip} to be the emission rate in the cavity, then the ratio $\mathcal{F} = \frac{\Gamma_{dip}}{\Gamma_0}$ is known as the Purcell factor of the SPE-cavity system. This value can be related to the power radiated by the dipole in vacuum, P_0 , and the power radiated by the dipole in the cavity, P_{dip} , where $\mathcal{F} = \frac{\Gamma_{dip}}{\Gamma_0} = \frac{P_{dip}}{P_0}$. This P_{dip} is made up of two components, the power that is radiated and the power that is lost due to nonradiative decay, denoted by P_{rad} and P_{loss} , respectively. We can thus define the quantum efficiency (QE) of the system to be $QE = \frac{P_{rad}}{P_{rad} + P_{loss}}$. If we are only interested in the power that is radiated to the far field, we can define the radiative enhancement as $\frac{P_{rad}}{P_0}$. This value quantifies the increase in radiated light that is able to be collected in the far field, normalized to the amount of far field light radiated by the SPE in vacuum.

It was first shown by Koppens and collaborators that it is possible to achieve strong coupling between a graphene nanodisk and an SPE.⁷⁴ The possibilities of engineering light-matter interaction via graphene nanodisks has been further explored including demonstration of Purcell enhancement of quadrupole transitions,⁷⁵ and a plasmon-plasmon interaction based the plasmon blockade effect.⁷⁶ It has also been shown by Cox and collaborators that the dipole-dipole interaction between a quantum well and a graphene nanodisk can be tuned via a nonlinear photonic crystal.⁷⁷ Alternative graphene geometries have shown promise in facilitating strong light-matter interaction as well, including a half-space graphene sheet which exhibits Purcell factors of up to 6 orders of magnitude⁷⁸ and nanoislands which can strongly enhance multipolar transitions to rates exceeding the dipole transition

rate.⁷⁹ In all cases presented above, the fluorescence enhancement is achieved by means of coupling to graphene surface plasmons (GSPs).

There have been several demonstrations of the Purcell enhancement of emission from defect-based emitters in hBN by means of plasmonic nanoantennas. These include multi-photon effects with intensity enhancements as large as 250,^{80,81} and single photon emission with intensity enhancements of 200%.⁸² These emitters make use of the negatively charged boron vacancy (V_B) in hBN, which has spin-dependent transitions⁸³ that can be controlled at room temperature.⁸⁴ These room-temperature spin-dependent transitions make this SPE a promising candidate for use in quantum technologies based on spin states^{85,86}.

Motivated by the exceptional ability of surface plasmons to boost radiative emission rates, we propose using *acoustic graphene plasmons* (AGPs) to realize *electrically tunable, giant* Purcell enhancements for single-photon, entangled-photon, and multipolar quantum emitters. Unlike graphene surface plasmons (GSPs) in extended sheets or localized surface plasmons (LSPs) in nanoantennas, AGPs concentrate the optical field in a nanogap cavity formed by a graphene sheet and a metallic nanocube, with a few-nanometer-thick dielectric spacer composed of stacked 2D layers that host defect/impurity-based quantum emitters.⁸⁷ Our finite-difference time-domain (FDTD) simulations show giant Purcell factors over a broad infrared window, reaching up to 10^6 in the mid-IR and up to 10^4 at telecommunications wavelengths, with corresponding quantum efficiencies as high as 95% (mid-IR) and 89% (telecom) for high-mobility graphene. At $\lambda = 1.55 \mu\text{m}$, we find Purcell enhancements of order 10^4 for electric-dipole (E1) transitions and up to 10^7 and 10^9 for electric-quadrupole (E2) and electric-octupole (E3) transitions, respectively (see Table I and Sec. VII in SI); remarkably, two-photon spontaneous emission (2PSE) transitions also reach $\sim 10^9$. Crucially, the AGP resonance is governed by the graphene Fermi energy and can thus be modulated via gate voltage, enabling real-time on-off control of the fluorescence enhancement (with large on-off ratios at telecommunications wavelengths) by shifting the AGP mode into or out of resonance with the emitter. As a concrete example, we analyze single- and two-photon spontaneous emission from Er³⁺ centers embedded in single-layer WS₂, demonstrating that AGP cavities provide a compact, CMOS-compatible route to high-brightness, high-efficiency, and *electrically tunable* quantum-light sources for quantum communication and information processing.

I. Results and discussion

AGP Resonances in the Heterostructure

The architecture of the AGP resonator is depicted in Fig. 1. We use an Ag nanocube with a side length of 50 nm placed upon one or more layers of hBN, a monolayer of Er-doped WS₂, and a graphene sheet. Underneath the graphene monolayer is a 1400 nm spacer made of SU-8 and an Au back

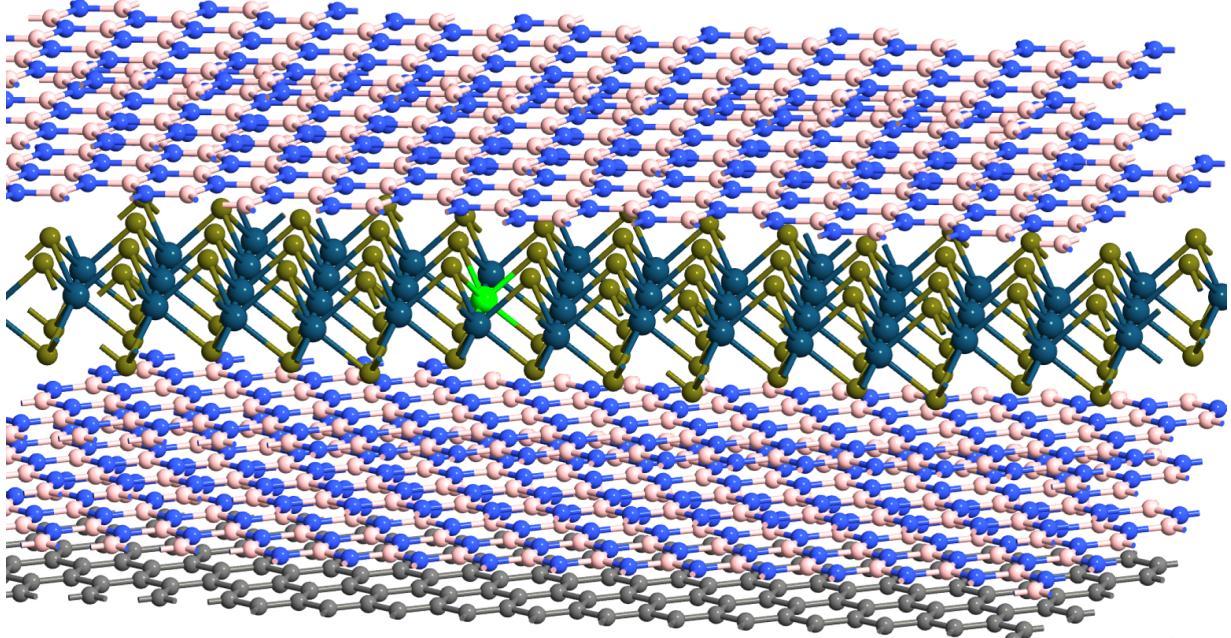


FIG. 2. Schematic diagram showing Er (green ball) doping in tungsten (dark blue ball) disulphide (mustard color ball). A layer of SL WS₂ is sandwiched between layers of hexagonal BN (pink and blue balls). Graphene layer (grey balls) is also shown at the bottom.

mirror. The AGPs are excited in the hBN/WS₂/hBN heterostructure (see Fig. 2) between the graphene sheet and the metal nanoparticle. The thickness h of the hBN/WS₂/hBN heterostructure, the number of graphene layers C_S with intercalated FeCl₃, and the Fermi energy E_F of the graphene layers were varied to tune the wavelength of the AGPs.

These AGPs induce an intense localized electrical field within the hBN/WS₂/hBN heterostructure. Here, we show that a single-photon emitter (SPE) in the form of erbium in WS₂ experiences a significant fluorescence enhancement effect due to the presence of these strong electric fields. These fields exist at the specific frequencies of the permitted AGP eigenmodes in the cavity. Consequently, fluorescence enhancement will selectively occur at these same frequencies. The AGP eigenmode frequencies of this cavity geometry have been predicted to follow the equation⁸⁸

$$f_{mn} = \sqrt{\alpha \frac{chE_F}{\pi^2 \hbar \epsilon_r}} \sqrt{\left(\frac{m\pi}{L}\right)^2 + \left(\frac{n\pi}{W}\right)^2} \quad (1)$$

where α is the fine structure constant and ϵ_r is the relative permittivity of the hBN/WS₂/hBN heterostructure. The variables L and W are the length and width of the cavity, respectively, which are defined by the size of the Ag nanocube.

To characterize the fluorescence enhancement induced by these AGPs, we simulate this device using the Ansys Lumerical finite-difference time-domain (FDTD) software. We model the SPE as an electric dipole located within the WS₂ monolayer. We study two cases: a dipole oriented perpendicular to the the graphene sheet, and a dipole oriented parallel to the graphene sheet.

For both the perpendicular and parallel cases, we see sev-

eral peaks in the Purcell factor corresponding to the allowed AGP eigenmodes in the cavity as depicted in Fig. 3 and Fig. 4. For the perpendicular orientation, a dipole emitter located at the geometric center of the hBN/WS₂/hBN heterostructure experiences a Purcell enhancement of several million. However, this monopole eigenmodes does not efficiently couple to the far field. As a result, we see radiative enhancement of less than 1 at the wavelength corresponding to this monopole. Suppose we instead shift the SPE's location in the x direction by $1/e$ of the side length of the nanocube. In that case, it is possible to excite a dipole E_z field inside the cavity that couples more strongly to the far field resulting in radiative enhancement. The remaining peaks in the Purcell enhancement spectrum correspond to higher order eigenmodes with weak far-field coupling.

For the parallel orientation, we are interested in the E_x field component rather than the E_z field component. Our FDTD calculations show the E_x field to be a monopole localized under the nanocubes. Thus, we observe a relatively small electric field present when offset from the center of the nanocube and a corresponding sharp drop in the radiative enhancement when compared to an electric dipole source located under the center of the nanocube.

Atom-plasmonic cavity system

The electric dipole emitter in the FDTD simulations models the spontaneous emission of an atom from the excited state $|e\rangle$ to its ground state $|g\rangle$. Since the electric dipole emitter is only a source of electromagnetic radiation, the FDTD simulations are valid in the weak coupling (Purcell) regime where the

re-absorption and re-emission cycles are neglected (see e.g. Refs. 89–91 for the detailed description of Rabi oscillations during the spontaneous emission process).

Both the enhancement and the suppression of the spontaneous emission of a quantum emitter can be derived from Fermi's golden rule,⁹²

$$\Gamma = \frac{2\pi}{\hbar^2} \left| \left\langle f \left| \hat{H}_{\text{int}} \right| i \right\rangle \right|^2 D(\omega) = 2\pi g^2(\mathbf{r}, \omega) D(\omega), \quad (2)$$

where $\hat{H}_{\text{int}} = -\hat{\mathbf{d}} \cdot \hat{\mathbf{E}}_{mn}$ is the perturbing interaction Hamiltonian, $|i\rangle$ and $|f\rangle$ are the initial and final states, respectively, and $g = \langle \hat{H}_{\text{int}} \rangle / \hbar$ is the coupling frequency between the quantum emitter's dipole moment $\hat{\mathbf{d}} = -e\hat{\mathbf{r}}$ and the electric field $\hat{\mathbf{E}}_{mn}$ of the AGP eigenmodes (m, n) . The dipole moment operator between the ground state $|g\rangle$ and excited state $|e\rangle$ of the quantum emitter is given by

$$\hat{\mathbf{d}} = |g\rangle \mathbf{d}_{ge} \langle e| + |e\rangle \mathbf{d}_{ge}^* \langle g|, \quad (3)$$

where $\mathbf{d}_{ge} = \langle g| \hat{\mathbf{d}} |e\rangle = -e \langle g| \hat{\mathbf{r}} |e\rangle$. The electric field operator is

$$\hat{\mathbf{E}}_{mn}(\mathbf{r}) = \mathbf{E}_{mn} a_{mn} + \mathbf{E}_{mn}^* a_{mn}^\dagger, \quad (4)$$

where a_{mn} and a_{mn}^\dagger are the annihilation and creation operators of the quantized AGPs in the eigenmodes (m, n) , respectively. The electric field components per single quantized AGP are given by⁸⁸

$$\begin{aligned} E_{mn,z}(\mathbf{r}) &= \sqrt{\frac{\hbar\omega_{mn}}{\epsilon_0\epsilon_r V_{mn}}} \sin(k_{mn,x}x) \sin(k_{mn,y}y) \cosh(\zeta_{mn,z}z) \\ E_{mn,x}(\mathbf{r}) &= \sqrt{\frac{\hbar\omega_{mn}}{\epsilon_0\epsilon_r V_{mn}}} \cos(k_{mn,x}x) \sin(k_{mn,y}y) \sinh(\zeta_{mn,z}z), \\ E_{mn,y}(\mathbf{r}) &= \sqrt{\frac{\hbar\omega_{mn}}{\epsilon_0\epsilon_r V_{mn}}} \sin(k_{mn,x}x) \cos(k_{mn,y}y) \sinh(\zeta_{mn,z}z), \end{aligned} \quad (5)$$

where the eigenfrequencies of the AGPs are $\omega_{mn} = 2\pi f_{mn}$, V_{mn} is the optical mode volume, and ϵ_r is the relative permittivity of the dielectric material between the Ag nanocube and graphene. The density of states (DOS) $D(\omega)$ represents the number of states per unit energy that the quantum emitter can decay into at the frequency ω . In vacuum the DOS in three dimensions is

$$D_0(\omega) = \frac{\omega^2 V}{\pi^2 c^3}, \quad (6)$$

where c is the speed of light in vacuum. Consequently, the spontaneous emission rate in vacuum is⁹²

$$\Gamma_0 = \frac{\omega^3 d_{ge}^2}{3\pi\epsilon_0\hbar c^3}. \quad (7)$$

Purcell realized that if the DOS is modified by a cavity, then

the spontaneous emission rate can be varied.⁹³ In the case of the AGP cavity the DOS is

$$D_{\text{AGP}}(\omega) = \frac{2}{\pi} \sum_{m,n} \frac{\gamma_{mn}}{4(\omega - \omega_{mn})^2 + \gamma_{mn}^2}, \quad (8)$$

where γ_{mn} are the linewidths of the Lorentzian peaks of the eigenmodes (m, n) . Thus, the spontaneous emission rate into AGP modes is

$$\Gamma(\mathbf{r}, \omega) = 4g^2(\mathbf{r}, \omega) \sum_{m,n} \frac{\gamma_{mn}}{4(\omega - \omega_{mn})^2 + \gamma_{mn}^2}. \quad (9)$$

After choosing a particular eigenmode (m_0, n_0) by setting $\omega \approx \omega_{m_0 n_0}$, one obtains the enhancement/suppression factor

$$\begin{aligned} F(\mathbf{r}, \omega) &= \frac{\Gamma(\mathbf{r}, \omega \approx \omega_{m_0 n_0})}{\Gamma_0} \\ &\approx \frac{3Q_{m_0 n_0} (\lambda_{m_0 n_0}/n)^3}{4\pi^2 V_{m_0 n_0}} \frac{\gamma_{m_0 n_0}^2}{4(\omega - \omega_{m_0 n_0})^2 + \gamma_{m_0 n_0}^2} \\ &\times \left(\frac{\mathbf{d} \cdot \mathbf{E}}{dE} \right)^2 \frac{|\mathbf{E}(\mathbf{r})|^2}{|\mathbf{E}_{\text{max}}|^2}, \end{aligned} \quad (10)$$

where $Q_{m_0 n_0} = \omega_{m_0 n_0} / \gamma_{mn}$ is defined as the quality factor of the eigenmode (m_0, n_0) . The prefactor of the above expression is the Purcell factor

$$\mathcal{F} \equiv F_{\text{max}} = \frac{3Q_{m_0 n_0} (\lambda_{m_0 n_0}/n)^3}{4\pi^2 V_{m_0 n_0}}, \quad (11)$$

which is achieved for exact resonance $\omega = \omega_{m_0 n_0}$, parallel or anti-parallel alignments of \mathbf{d} and \mathbf{E} , i.e. $\mathbf{d} \cdot \mathbf{E} = \pm dE$, and maximum electric field $\mathbf{E}(\mathbf{r}) = \mathbf{E}_{\text{max}}$.

Weak and strong-coupling regimes

Eq. (10) derived above is valid for the weak-coupling regime, in which $g < \kappa, \Gamma_0$. In the strong-coupling regime, the emitted photon goes through several reabsorption and re-emission cycles, resulting in damped Rabi oscillations with a rate g . A quantum treatment gives the equation

$$\Gamma = \Gamma_0 + \frac{4g^2}{\kappa} \quad (12)$$

which we can rewrite in terms of the Purcell factor $\mathcal{F} = \frac{\Gamma}{\Gamma_0}$ as

$$\mathcal{F} = 1 + \frac{4g^2}{\kappa\Gamma_0} \quad (13)$$

We can find the value of κ for a given eigenmode from its frequency and quality factor as

$$\kappa = \frac{\omega_{m_0 n_0}}{Q_{m_0 n_0}} \quad (14)$$

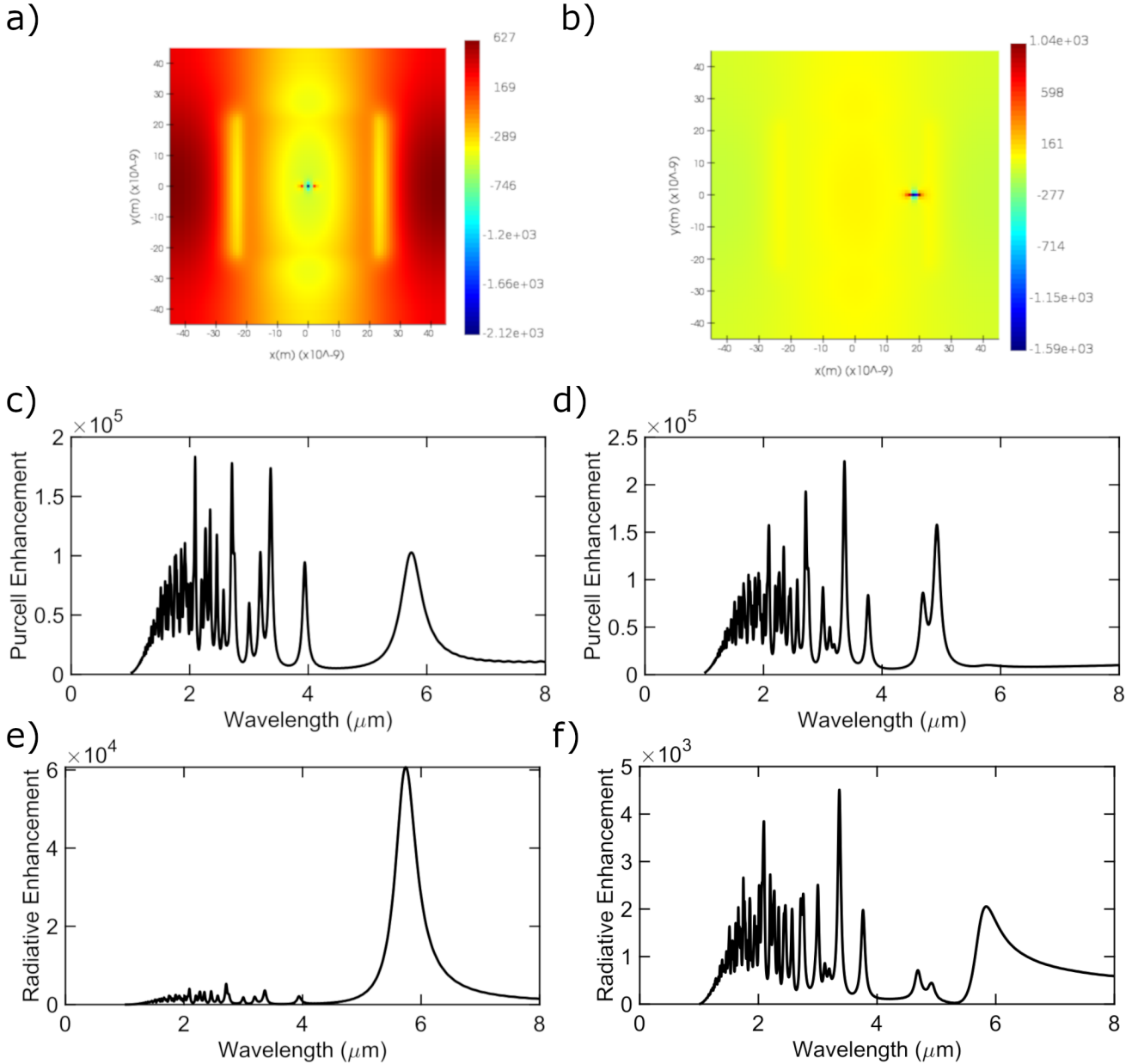


FIG. 3. E_X field of the AGP at the center of the heterostructure cavity with respect to the z-axis for the case when the dipole is oriented parallel to the graphene layer and placed both a) on resonance at $x = 0$ nm and b) off resonance at $x = 18$ nm. A large Purcell enhancement is seen c) on resonance and also d) off resonance. We see that the radiative enhancement e) on resonance is significantly larger than f) off resonance as well. This is because when the dipole is on resonance, it is located near the maximum value of E_X , whereas when off resonance it is located near a local minima of E_X .

We can then solve for g/κ as

$$\frac{g}{\kappa} = \sqrt{\frac{(\mathcal{F} - 1)\Gamma_0}{4\kappa}} = \sqrt{\frac{(\mathcal{F} - 1)\Gamma_0}{4} \frac{Q_{m_0n_0}}{\omega_{m_0n_0}}}, \quad (15)$$

which is a useful reformulation of Eq. (10) as we can easily distinguish between the strong coupling regime ($g/\kappa > 1$) and the weak coupling regime ($g/\kappa < 1$). For the IR cavity with a resonant frequency of $\omega_{m_0n_0} = 3.28 \times 10^{14}$ rad/s, correspond-

ing to a frequency of $f_{m_0n_0} = \omega_{m_0n_0}/2\pi = 52.1$ THz and a wavelength of $\lambda_{m_0n_0} = 5.75$ μm , we have $\kappa = 3.9 \times 10^{12}$ s⁻¹ and $\mathcal{F} = 2.75 \times 10^6$, and therefore

$$\frac{g}{\kappa} = 4.2 \times 10^{-4} \sqrt{\Gamma_0}. \quad (16)$$

Similarly, for the telecommunications wavelength cavity we have a resonant frequency of $\omega_{m_0n_0} = 1.22 \times 10^{15}$ rad/s, corresponding to a frequency of $f_{m_0n_0} = \omega_{m_0n_0}/2\pi = 193$ THz and

a wavelength of $\lambda_{m_0n_0} = 1.55 \mu\text{m}$, we have $\kappa = 1.26 \times 10^{13} \text{ s}^{-1}$ and $\mathcal{F} = 1.76 \times 10^4$, and therefore

$$\frac{g}{\kappa} = 1.9 \times 10^{-5} \sqrt{\Gamma_0}. \quad (17)$$

Thus, we see that the strong coupling regime can be reached as long as the vacuum decay rate of the transition $\Gamma_0 \gtrsim 5.7 \times 10^6 \text{ s}^{-1}$ for $\lambda_{m_0n_0} = 5.75 \mu\text{m}$, and $\Gamma_0 \gtrsim 2.3 \times 10^9 \text{ s}^{-1}$ for $\lambda_{m_0n_0} = 1.55 \mu\text{m}$.

Electrostatic tuning of AGP frequency

It has been reported that the frequency of these AGPs can be tuned by means of a gate voltage applied to the graphene sheet.⁸⁸ This gate voltage varies the Fermi energy of the graphene sheet and in turn the frequency of the AGP. We vary the Fermi energy in the FDTD simulation and change the corresponding scattering rate according to

$$\tau^{-1} = \frac{ev_F^2}{\mu E_F} \quad (18)$$

where $v_F = 10^6 \text{ m/s}$ is the Fermi velocity of graphene and μ is the mobility of the graphene sheet. This equation can also be rewritten in the standard form $\mu = ev_F^2 \tau / E_F$. We vary the Fermi energy from $E_F = 0.8 \text{ eV}$ to 1.2 eV , while the thickness h of the hBN/WS₂/hBN heterostructure is fixed at 5 nm, and a single graphene layer is present. When varying E_F , the frequency of the AGP resonances closely follows the square root dependence of f_{AGP} on E_F as shown in Fig. 5 and predicted in Eq. (1). This method of tuning has the distinct advantage of being able to be varied in real time. In contrast, the thickness of the hBN/WS₂/hBN heterostructure and the number of graphene layers are fixed after device fabrication. We see that the AGP can be tuned electrostatically by approximately $2 \mu\text{m}$ by varying E_F from 0.6 eV to 1.2 eV . This electrostatic tunability can be used to switch the Purcell enhancement on and off in real time by means of varying the applied gate voltage. By tuning between $E_F = 0.6 \text{ eV}$ to $E_F = 1 \text{ eV}$ we are able to achieve an on-off ratio of 19.7 dB in the radiative enhancement of the device.

Geometric tuning of AGP frequency

The AGP frequency is predicted to show a square root dependence on the thickness of the hBN/WS₂/hBN heterostructure according to Eq. (1). We calculate the AGP frequency using Lumerical FDTD and vary the thickness of the hBN/WS₂/hBN heterostructure from 1 nm to 10 nm. We fix the Fermi energy at $E_F = 1 \text{ eV}$ and use a single graphene layer. We see in Fig. 5 that the rate of increase in frequency of the AGP resonances decreases rapidly from the expected square root dependence at larger thickness of the hBN/WS₂/hBN heterostructure. However, as this thickness decreases, we approach the expected square root dependence.

In addition, we propose using multi-layered graphene to

further increase the frequency of the AGPs. This is accomplished using multiple layers of graphene intercalated with FeCl₃. With this method, the distance between the graphene layers is increased resulting in very weak interactions between the graphene layers.⁹⁴ As a result, we expect the total conductivity of the multi-layer graphene intercalated with FeCl₃ to scale with the number of graphene layers. The AGP frequency has been shown to scale with the square root of the total conductivity of graphene.⁹⁵ As a result, we expect the AGP frequencies to scale with the square root of the number of graphene layers C_S . We vary C_S in the Lumerical FDTD simulation and observe the change in AGP frequency and Purcell enhancement factor \mathcal{F} . We see that for the dipole AGP eigenmode, the relationship between AGP frequency and C_S scales with a near square root relationship.

Effects of tuning methods on enhancement factor

While all three of the presented methods for tuning the AGP frequency scale with a near square-root dependence, they differ in how they affect the magnitude of the enhancement factor. The radiative transition rates and Purcell enhancement factors as a function of E_F , h , and C_S for the perpendicular dipole orientation are shown in Fig. 6. In general, we see that increasing the frequency of the AGP decreases the enhancement factor experienced by the dipole source. Although increasing the value of C_S and h initially result in a large decrease in enhancement, we see that both reach a point at which further increases have diminishing effects on enhancement. This is promising as it allows us to greatly increase the frequency of the AGPs while maintaining a high enhancement rate, which, as we see later, allows us to reach telecommunications wavelengths while maintaining a large Purcell enhancement.

Example of frequency tuning to 1550 nm

To demonstrate the tuning capability of the proposed heterostructure, we tune the AGP resonance to 1550 nm as shown in Fig. 7. For the hBN/WS₂/hBN heterostructure, we use a thickness of 10 nm, $C_S = 10$ graphene layers, and $E_F = 1.2 \text{ eV}$. As noted previously, achieving this high frequency results in a reduction in the enhancement factors. Using the aforementioned parameters, we achieved an AGP wavelength of 1550 nm with a Purcell enhancement factor of $\mathcal{F} = 1.76 \times 10^4$ and a quantum efficiency of $QE = 0.79$ for a total radiative enhancement factor of $\xi_{\text{ON}} = \mathcal{F}QE = 1.39 \times 10^4$. We can shift the AGP frequency, and therefore the peak in enhancement, to higher wavelengths by decreasing the Fermi energy. Doing so allows for the enhancement of the 1550 nm electric dipole to be effectively switched on and off. By setting the Fermi energy to $E_F = 0.75 \text{ eV}$, we can reduce the radiative enhancement factor to $\xi_{\text{OFF}} = 40.36$. This means that the radiative

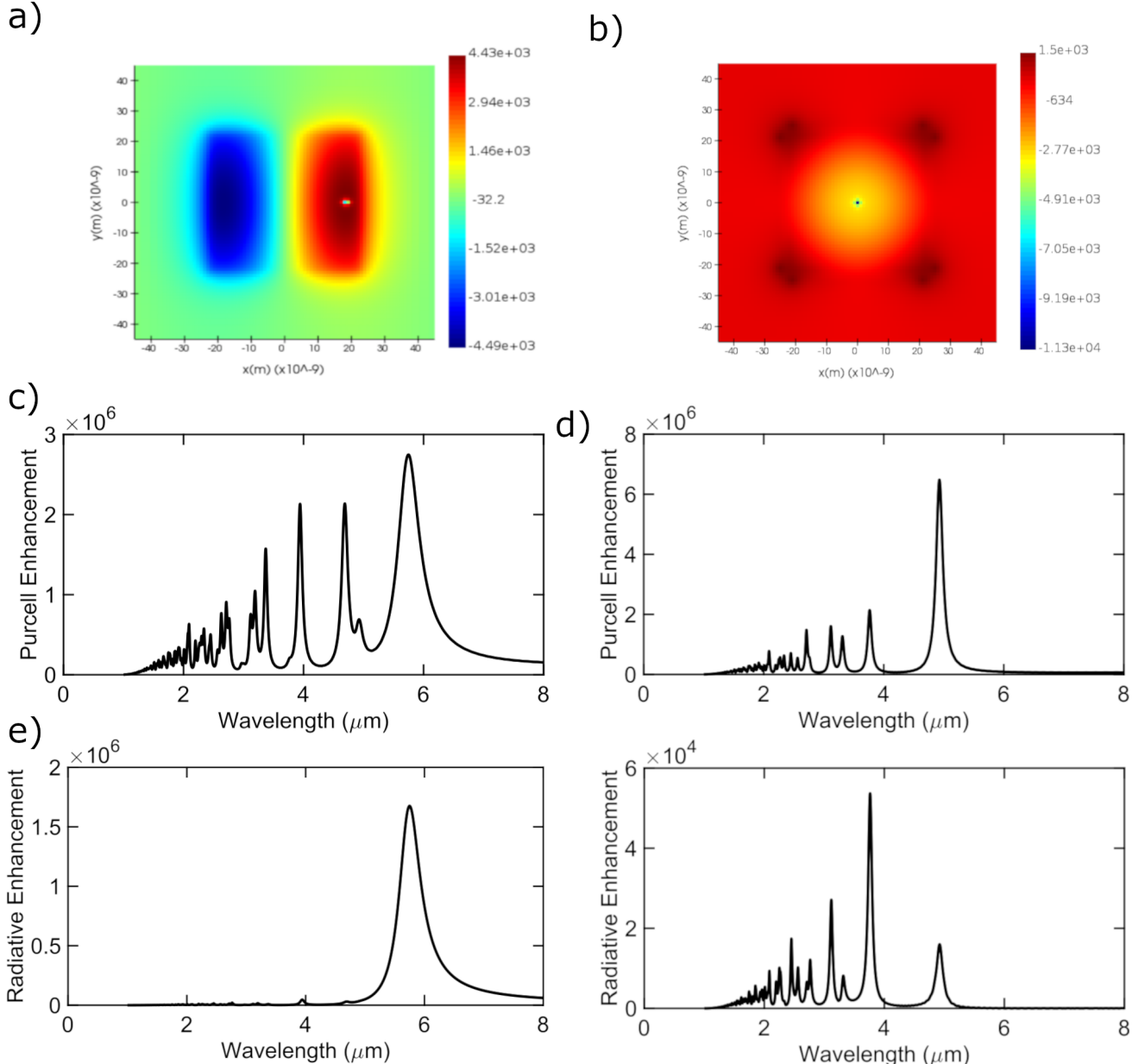


FIG. 4. E_z field of the AGP at the center of the heterostructure cavity with respect to the z-axis for the case when the perpendicular dipole is placed both a) on resonance at $x = 18$ nm and b) off resonance at $x = 0$ nm. A large Purcell enhancement is seen for both c) off resonance and d) on resonance with both having a similar magnitude. However, we see that the radiative enhancement is much larger e) on resonance while radiative enhancement is much lower f) off resonance as the monopole excited by the dipole at $x = 0$ nm does not couple strongly to the far field while the dipole resonances excited by the dipole at $x = 18$ nm couples efficiently to the far field. This shows that the efficiency of the Purcell enhancement is highly dependent on the location of the emitter relative to the electric field distribution of the AGP.

enhancement factor can be varied by a factor of

$$\frac{\xi_{\text{ON}}}{\xi_{\text{OFF}}} = 3.44 \times 10^2 \quad (19)$$

between the on and off modes of operation, which is equivalent to $10\log_{10}(\xi_{\text{ON}}/\xi_{\text{OFF}}) = 25.4$ dB.

Effects of graphene mobility on QE

The previous results in this study have assumed a graphene mobility of $\mu = 2000 \text{ cm}^2/\text{Vs}$, which is a relatively conservative value for modern fabrication methods. Graphene mobilities of up to $\mu = 125,000 \text{ cm}^2/\text{Vs}$ have been reported in hBN encapsulated graphene⁹⁶, and up to $\mu = 10,000 \text{ cm}^2/\text{Vs}$ using scalable fabrication methods⁹⁷. We expect that using a higher

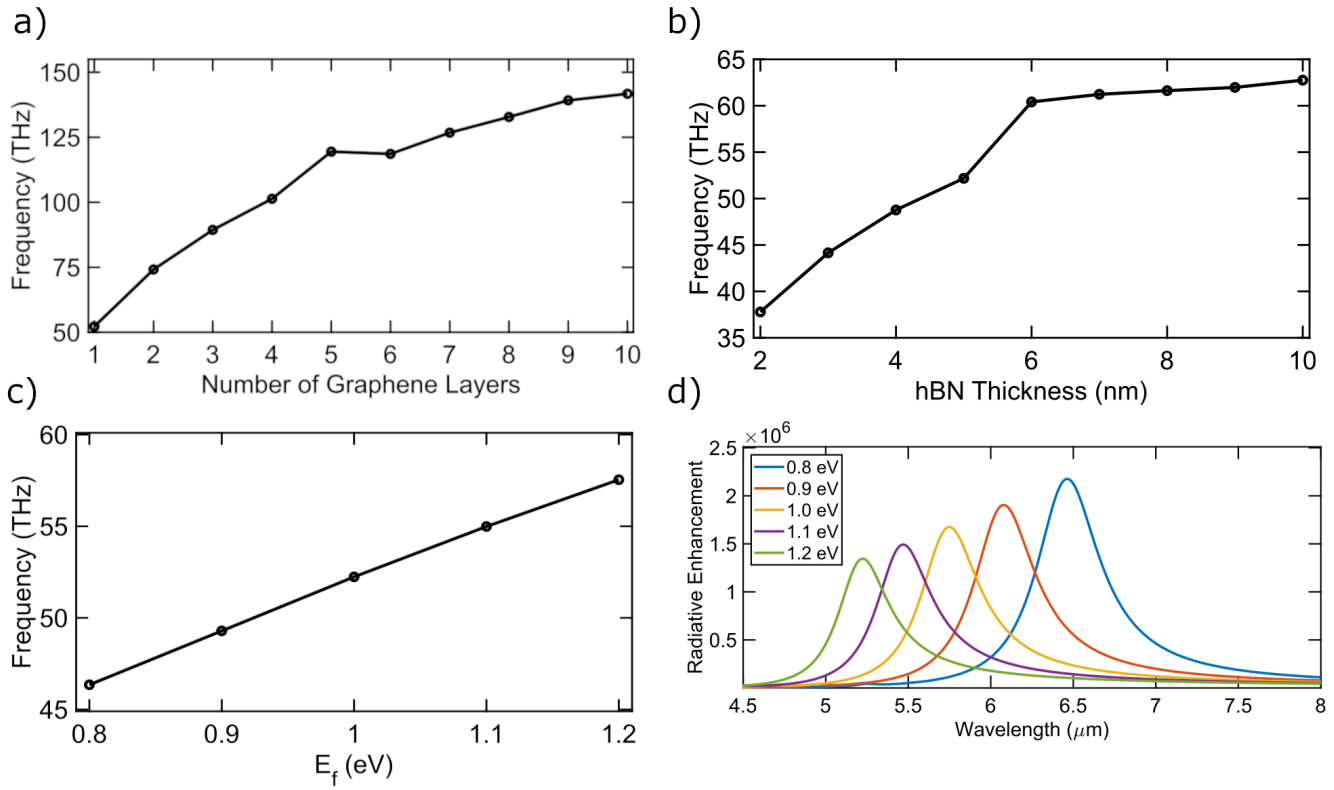


FIG. 5. Near square root relationship between the frequency of the excited AGP in the cavity as a function of a) number of graphene layers intercalated with FeCl_3 (C_S), b) hBN layer thickness (h), and c) graphene Fermi energy (E_F) for the perpendicular dipole orientation. The radiative enhancement factor as a function of wavelength is shown for d) multiple values of E_F as well to clearly demonstrate the electrostatic tunability of the AGPs. When not the variable of interest, we set $C_S = 1$, $E_F = 1.0$ eV, and $h = 5$ nm.

mobility increases the QE of the device. In Fig. 8, we see that increasing the mobility to $\mu = 10,000 \text{ cm}^2/\text{Vs}$ results in a $QE = 92.4\%$ for $\lambda = 5.75 \mu\text{m}$ and $QE = 89\%$ for $\lambda = 1.55 \mu\text{m}$. This increase in quantum efficiency QE is vital for creating high quality single photon and entangled photon sources, as it directly determines the value of β_{ext} . In summary, this shows that high quantum efficiency QE is achievable in AGP resonances if high mobility graphene is used. We expect that the QE must saturate at some point, as it can never exceed 100%. Thus, we fit the data to a function of the form $1 - e^{-x}$. This analysis suggests that the quantum efficiency QE of the device optimized for $\lambda = 5.75 \mu\text{m}$ saturates at 95% and for the $\lambda = 1.55 \mu\text{m}$ device QE saturates at 89% as shown in Fig. 9.

Extension to electric and magnetic multipolar and nonlinear optical transitions

The Lumerical FDTD software does not contain methods for simulating multipolar transitions, two-plasmon spontaneous emission, or spin-flip transitions. However, it has been shown that the magnitude of fluorescence enhancement for the electric dipole transition can be used to calculate the en-

hancement of these other emission processes⁹⁸. The rate enhancement of each transition is calculated from a characteristic value η according to the equations shown in Table I. We see that the equation for the enhancement of the electric dipole ($E1$) transition is equal to η^3 , and we can thus extract the value of η as the cube root of our Purcell enhancement factor, i.e.

$$\eta = \mathcal{F}^{\frac{1}{3}}. \quad (20)$$

Using this identity, we can calculate the enhancement rate of the other transition types based on the characteristic equation of that transition using our value of η . Examples are given in Table I for two different wavelengths. The enhancement factors for the multipolar and higher-order transitions are much larger than for the electric dipole transition, enabling the measurement of transitions that are not typically visible experimentally.

Dark and bright modes in the AGP cavity

Of the several modes supported by the AGP cavity, only one of these modes is bright while the others are dark, i.e. the dipole AGP mode is the sole bright mode. This mode

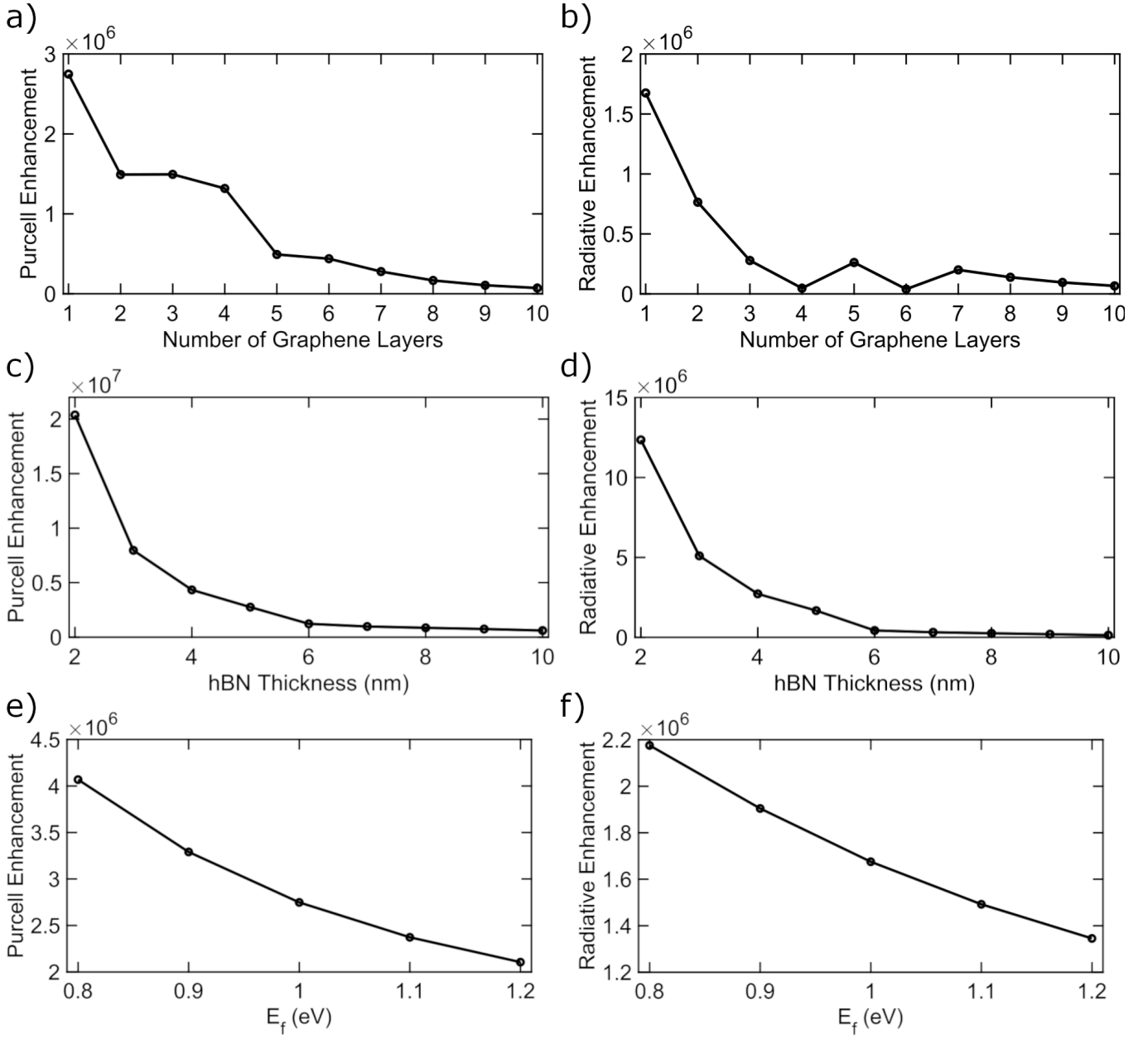


FIG. 6. Relationship between the number of intercalated graphene layers (C_s) and the a) peak Purcell enhancement and b) peak radiative enhancement. Relationship between the hBN layer thickness (h) and the c) peak Purcell enhancement and d) peak radiative enhancement. Relationship between the graphene Fermi energy and the e) peak Purcell enhancement and f) peak radiative enhancement. When not the variable of interest, we set $C_s = 1$, $E_F = 1.0$ eV, and $h = 5$ nm.

couples strongly to the far-field with quantum efficiencies QE of up to 90%. In contrast, the next higher order modes are dark modes. These dark modes only couple a small fraction of emitted energy to the far-field. The remaining energy emitted by dark modes is primarily coupled into decaying plasmon modes. This energy decays into vibrational modes that dissipate as heat into the graphene layer. It has been shown that when multiple plasmon cavities are in close proximity, it is possible to have couplings between plasmons that result in the shifting of the plasmon frequencies, or even splitting into

two hybridized modes.⁹⁹ While we do not observe this splitting for the bright dipole mode, the higher order dark plasmon modes do exhibit this splitting. The frequency difference of these peaks is constant with respect to the vacuum decay rate of the emitter, suggesting that this is indeed due to plasmon hybridization and not strong coupling between the SPE and the plasmon cavity.

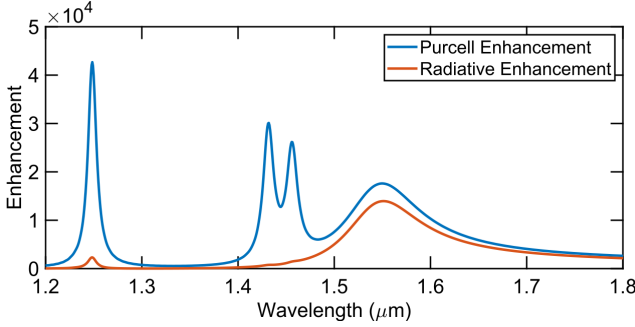


FIG. 7. Demonstration of tuning of electric dipole emission for $C_S = 10$, $h = 10$ nm, and $E_F = 1.2$ eV to enable operation in the C band at 1550 nm with a Purcell enhancement of 1.76×10^4 .

Purcell Enhancement Factors for Various Transition Types			
Optical Transition	Enhancement Factor Formula	Enhancement Factor Value $\lambda = 5.75 \mu\text{m}$	Enhancement Factor Value $\lambda = 1550 \text{ nm}$
$E1$	$\mathcal{F} = \eta^3$	2.75×10^6	1.76×10^4
$E2$	$\eta^{3+2(n-1)}$	5.4×10^{10}	1.19×10^7
$E3$	$\eta^{3+2(n-1)}$	1.06×10^{15}	8.06×10^9
$2PSE$	η^6	7.56×10^{12}	3.1×10^8
$M1$	$\eta^{1+2(n-1)}$	140.1	26.0
$M2$	$\eta^{1+2(n-1)}$	2.75×10^6	1.76×10^4
$M3$	$\eta^{1+2(n-1)}$	5.4×10^{10}	1.19×10^7

TABLE I. Enhancement rates and rate equations for several transition types including multipolar electric ($E1$: electric dipole, $E2$: electric quadrupole, $E3$: electric octupole), magnetic ($M1$: magnetic dipole, $M2$: magnetic quadrupole, $M3$: magnetic octupole), and 2-photon spontaneous emission ($2PSE$) based on electric dipole ($E1$) matrix elements. The order of the multipolar transition in the enhancement factor is identified by n .

Potential applications

Telecommunication bands used in optical fibers

Rare-earth atoms have been used for classical communication in the telecommunication bands shown in Table II.

Band	Wavelength [nm]	Description
O	1260–1360	Original band
E	1360–1460	Extended band
S	1460–1530	Short wavelength band
C	1530–1565	Conventional band
L	1565–1625	Long wavelength band
U	1625–1675	Ultralong wavelength band

TABLE II. Standard bands for optical fiber communications

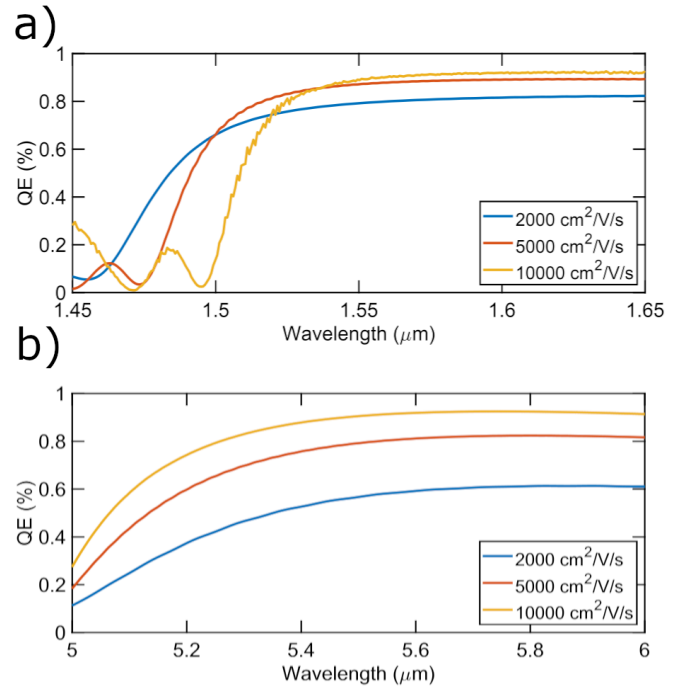


FIG. 8. Quantum efficiency of the cavity for a resonance centered at (a) $1.55 \mu\text{m}$ and (b) $5.75 \mu\text{m}$.

Single-photon source based on electric dipole transitions in rare-earth-doped TMDs

It has been shown that rare-earth doped 2D TMDs are candidates for photoluminescence sources in the NIR region, including at 1550 nm.^{71,100,101} It is possible to dope WS₂ with Er, where the Er ions are substituted into the WS₂ structure by replacing W cations. This Er:WS₂ material exhibits a fluorescence transition at approximately 1550 nm^{71,101,102}. We propose to use our hBN/WS₂/hBN heterostructure with this Er:WS₂ material as shown in Fig. 2. Similar results can be expected for hBN/MX₂/hBN heterostructure, where M=Mo, W is the transition metal atom, and X=S, Se is the chalcogen atom. We then expect this fluorescence transition to have a greatly enhanced transition rate.

First we show that Er:WS₂ indeed shows a transition at 1.5 microns by using first principle methods. All numerical calculations are performed using density functional theory (DFT) with the hybrid generalized gradient approximation (GGA) in the form of the HSE functional, as implemented in the Synopsis Atomistix Toolkit (ATK) 2022.¹⁰³ In hybrid GGA methods, a portion of the Hartree–Fock exchange is combined with the GGA exchange-correlation functional. This mixing fraction is typically denoted by " α ", with values ranging from 0 (pure GGA) to 1 (pure Hartree–Fock). In this work, we employ the standard HSE06 hybrid functional parameters ($\alpha = 0.25$). The inclusion of Hartree–Fock exchange in hybrid GGA calculations leads to an improved description of electronic properties such as band gaps, which are often underestimated in conventional GGA approaches. The system

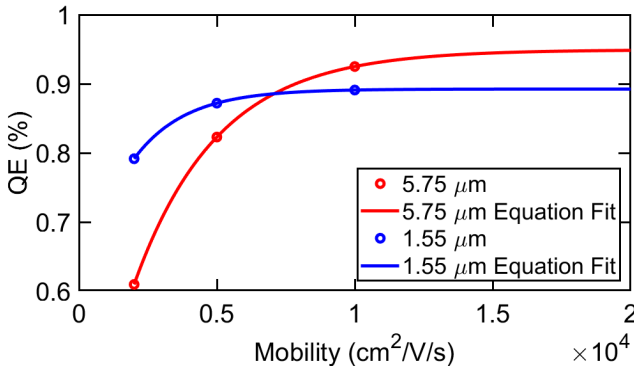


FIG. 9. Quantum efficiency of the cavity for a resonance centered at $1.55\ \mu\text{m}$ and $5.75\ \mu\text{m}$ as a function of the graphene mobility along with best fit equations.

under consideration is modeled using a supercell of WS_2 comprising 63 W atoms, 128 S atoms, and one substitutional Er impurity (Er_W). A vacuum layer of 25 Å is included to screen interlayer interactions. Prior to the electronic structure calculations, the atomic positions in the supercell are fully relaxed until the maximum force on each atom is below 0.01 eV/Å.

The band structure and the density of states for the Er doped SL WS_2 are shown in the Fig. 10. The projected bandstructure and density of states on 4f orbitals are also shown Fig. 10 (a) (blue color), appearing as dispersionless atomic like impurity states. Also, a finite contribution of 5d-orbitals (red color) can also be seen along with the f-orbitals in the density of states plot. Er ions have a characteristic signature emission in the $1.5\ \mu\text{m}$ (0.82 eV) range and have been reported in various studies involving Er dopants in semiconductors and insulators.^{102,104} Remarkably we are able to reproduce the characteristic radiative transition between different 4f orbitals of Er in the optical spectrum Fig. 10 (b) as T_1 at 0.82 eV (~ 1.52 microns). The appearance of characteristic emission of Er in different crystal environments such as SL WS_2 shows the minimum coupling of 4f orbitals of Er with the host material such as SL WS_2 .

Radiative transitions among f -orbitals have been extensively investigated since the 1960s, as such processes are nominally forbidden by electric dipole selection rules. The Judd–Ofelt theory^{105,106} provides a framework to describe these transitions by introducing odd-parity terms into the crystal-field Hamiltonian, which arise only in non-centrosymmetric crystal environments. Within the second-order perturbation framework, it has been shown that f -orbitals can hybridize with 5d-orbitals, i.e., $\langle f | \hat{H}_\text{cry} | d \rangle \neq 0$, only when \hat{H}_cry contains odd-parity components—thus enabling otherwise forbidden radiative transitions. In the present case, the Er impurity in WS_2 occupies a site of D_{3h} symmetry, which lacks inversion symmetry and therefore allows odd terms in the crystal-field Hamiltonian. The corresponding crystal-field potential can be expressed as

$$\hat{H}_\text{CF} = B_2^0 \hat{O}_2^0 + B_3^3 \hat{O}_3^3 + B_4^0 \hat{O}_4^0 + \dots \quad (21)$$

The odd-parity component $B_3^3 \hat{O}_3^3$ arises exclusively from the

non-centrosymmetric nature of the D_{3h} point group and is responsible for mediating the coupling between the 4f and 5d orbitals of Er, as reflected in the blue and red features of the density of states shown in Fig. 10(a).

Using the Kohn-Sham states, we can calculate the spontaneous emission rate for the fluorescence transition at about 1550 nm. The spontaneous emission rate of a photon can be derived using Fermi's golden rule, as shown in the Supplementary Information. We use the following relation to calculate the single-photon emission rate $1/\tau$

$$\frac{1}{\tau} = \frac{4}{3\epsilon_r^\perp} \left(\frac{e^2}{4\pi\epsilon_0\hbar c} \right) \left(\frac{\omega_{3,6}^3}{c^2} \right) |\langle 3 | z | 6 \rangle|^2 \quad (22)$$

$\omega_{3,6}$ denotes the frequency of radiation corresponding to the transition from level $|6\rangle$ to level $|3\rangle$, as illustrated in Fig. 10(a), while $\langle 3 | z | 6 \rangle$ represents the electric dipole matrix element between the electronic states $|6\rangle$ and $|3\rangle$. Within the electric dipole approximation, the calculated spontaneous emission rate for this transition is found to be $1/\tau = 2.6 \times 10^5\ \text{s}^{-1}$. Inserting this value for $\Gamma_0 = 1/\tau$ in Eq. (15), we obtain $g/\kappa = 0.01$, which is clearly in the Purcell regime.

Based on our Purcell enhancement factor of $1.76 \times 10^4 \sim 1550\ \text{nm}$, we can reduce this lifetime to $2.185 \times 10^{-10}\ \text{s}$. However, we must note that the quantum efficiency is also reduced by a factor of 0.788. This gives an effective radiative lifetime of $2.77 \times 10^{-10}\ \text{s}$. This large, tuneable radiative enhancement has the potential to be used to modulate the intensity of emitted light at 1550 nm, making it a promising candidate for use in fiber optic telecommunication systems. In particular, rare-earth atoms have typically very long lifetimes. Our heterostructure shows that these long lifetimes can be reduced by factors of the order of 10^4 .

Single-photon source based on weakly Purcell-enhanced magnetic dipole transitions in rare-earth-doped TMDs

Magnetic dipole (M1) transitions in rare-earth atoms have typically very long lifetimes, making them very challenging to observe experimentally. Inspecting the tables of M1 transitions in rare-earth atoms in Ref. 107, we can identify the following M1 transitions with vacuum rates $> 1.0\ \text{s}^{-1}$ and wavelengths $1400\ \text{nm} < \lambda < 1700\ \text{nm}$ that can be enhanced by means of AGPs. According to Table I, we obtained an estimate of the Purcell enhancement factor of $\mathcal{F}_{\text{M1}} = 37.5$. This results in relatively weakly Purcell-enhanced M1 emission rates, shown in Sec. VII in SI.

Single-photon source based on strongly Purcell-enhanced electric quadrupole transitions in rare-earth-doped TMDs

Electric quadrupole (E2) transitions involve a change in angular momentum of two units, which cannot be accounted for by the photon's spin alone. To conserve total angular momentum, the emitted photon must carry orbital angular momentum (OAM) in addition to its intrinsic spin, i.e. $J = 2$. This angu-

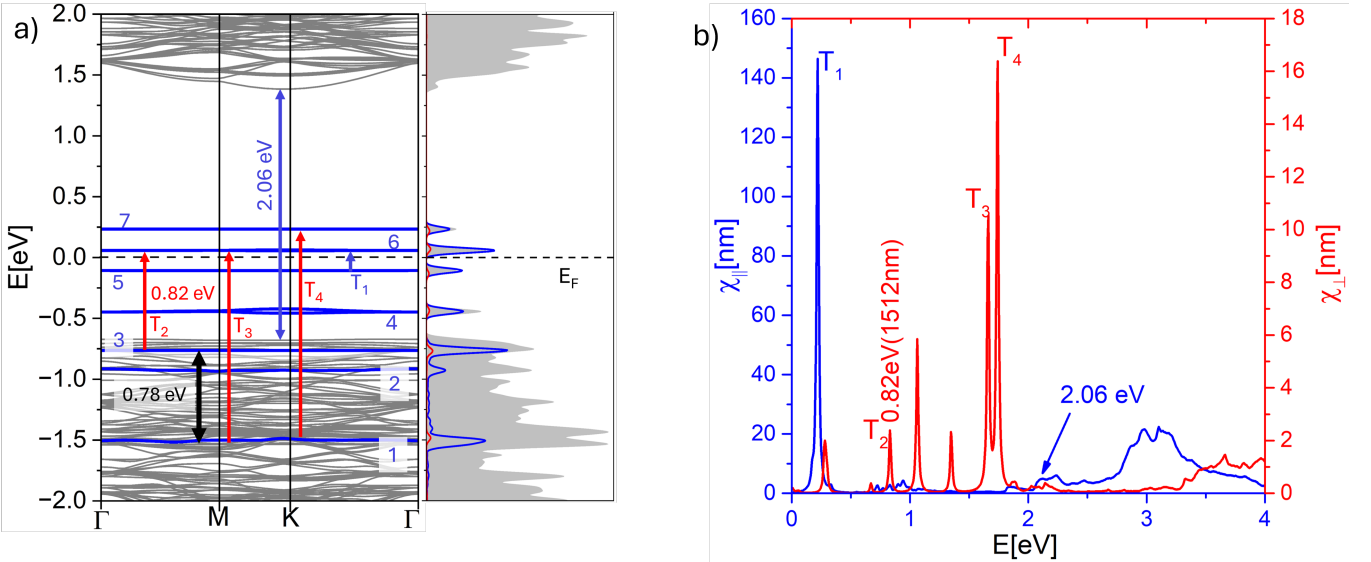


FIG. 10. Band structure, density of states (DOS), and optical spectrum of Er-doped single-layer WS₂. The blue horizontal lines in the band structure and the blue peaks in the DOS represent the localized 4f impurity states of Er. The red curves in the DOS indicate the finite contribution from the Er 5d orbitals, while the shaded grey region denotes the total DOS. Colored vertical arrows mark representative optical transitions between localized defect states (LDS) observed in the susceptibility tensor, corresponding to in-plane (blue) and out-of-plane (red) polarization components.

lar momentum arises from the spatial structure of the electromagnetic field, such as helical phase fronts in the emitted light. Photons with OAM are important because they enable access to higher-order transitions, allow for encoding information in new degrees of freedom,¹⁰⁸ and are essential in advanced applications like quantum communication^{109,110} and high-resolution spectroscopy. Understanding and utilizing this angular momentum opens new frontiers in light–matter interaction and photonic technologies.

Electric quadrupole (E2) transitions in rare-earth atoms have typically very long lifetimes, making them very challenging to observe experimentally.

We found above that we can achieve a Purcell enhancement rate of $\mathcal{F} = 1.76 \times 10^4$ at 1550 nm for the electric dipole (E1) transition. From this, we find the quadrupole Purcell enhancement to be 1.19×10^7 .

Inspecting the tables of E2 transitions in rare-earth atoms in Ref. 107 (see Sec. VII in SI), we can identify the following E2 transitions with vacuum rates of the orders of 10^{-5} s^{-1} to 10^{-4} s^{-1} and wavelengths $1400 \text{ nm} < \lambda < 1700 \text{ nm}$ that can be enhanced by means of AGPs. According to Table I, we obtained an estimate of the Purcell enhancement factor of $\mathcal{F}_{\text{E2}} = 1.19 \times 10^7$. This results in giant Purcell-enhanced E2 emission rates shown in Sec. VII in SI, ranging between 154 s^{-1} and 4573 s^{-1} .

Entangled-photon source based on rare-earth atoms in TMDs

2-photon electric dipole (2PSE) transitions can result in the emission of two entangled photons. These transitions are possible in rare-earth atoms in TMDs at wavelengths of inter-

est to telecommunications^{111,112}. As discussed previously, we can predict the Purcell enhancement rate of these transitions based on our simulated Purcell enhancement rate of the dipole transition⁹⁸. For 2PSE transitions, it has been predicted that Erbium has a 2PSE transition with a vacuum decay rate of $2.943 \times 10^{-7} \text{ s}^{-1}$ at a wavelength of $\lambda = 3.1 \mu\text{m}$.

Using the Purcell enhancement factor for localized AGPs, we obtain that the Purcell enhancement for a 2PSE emitter at $\lambda = 3.1 \mu\text{m}$ is of the order of 10^{12} , two orders of magnitude larger than for the case of graphene only (see Ref. 111).

Entangled Photon Emission at telecommunications wavelengths

The energy difference between the states $|6\rangle$ and $|3\rangle$ is 0.82 eV while the energy difference between $|3\rangle$ and $|1\rangle$ is 0.78 eV, as shown in Fig. 10. This 3 level system can be employed for a two-photon emission with intermediate energies i.e. $\hbar\omega + \hbar\omega' = 1.6 \text{ eV}$, by considering $|3\rangle$ as the intermediate state. We use a second order time dependent perturbation theory to calculate the two-photon emission decay rate i.e. (see SI)

$$\frac{1}{\tau^{(2)}} = 128\pi^5 \left(\frac{e^2}{\sqrt{\epsilon_{\parallel}\epsilon_{\perp}}\hbar c} \right)^2 \left(\frac{\omega_{63}^5}{c^4} \right) \left| \langle 1|x_{\parallel}|3\rangle \langle 3|x_{\perp}|6\rangle \right|^2 \times \int_0^2 \frac{x(2-x)}{(1-x)^2} dx \quad (23)$$

The matrix elements $\langle p|x_{\parallel(\perp)}|q\rangle$ were obtained from first-principles calculations. Using the values, the two-photon emission rate was calculated to be $9.127 \times 10^{-5} \text{ s}^{-1}$. By in-

corporating the Purcell enhancement factor 3.1×10^8 and accounting for a reduction in the quantum yield, the corresponding two-photon emission rate becomes $\frac{1}{\tau^{(2)}} = 2.23 \times 10^4 \text{ s}^{-1}$, which corresponds to a lifetime of $\tau^{(2)} = 4.49 \times 10^{-5} \text{ s}$. This large, tunable radiative enhancement enables modulation of the emission intensity $\sim 1550 \text{ nm}$, positioning the system as a strong candidate for integration into fiber-optic telecommunication technologies.

Cooperativity and β -factor

The total radiative enhancement factor ξ accounts for both the Purcell enhancement factor \mathcal{F} and the quantum efficiency QE . The Purcell enhancement factor \mathcal{F} describes the enhancement of the radiative decay rate due to the presence of an optical cavity, i.e.

$$\mathcal{F} = \frac{\Gamma_{\text{rad}}}{\Gamma_{\text{rad}}^0}. \quad (24)$$

Thus, the total radiative enhancement factor is given by

$$\xi = \mathcal{F}QE = \frac{\Gamma_{\text{rad}}}{\Gamma_{\text{rad}}^0} \cdot \frac{\Gamma_{\text{rad}}}{\Gamma_{\text{rad}} + \Gamma_{\text{loss}}} \quad (25)$$

This factor represents the combined effect of the Purcell enhancement and the quantum efficiency in determining the overall radiative enhancement of the quantum emitter.

The cooperativity and β -factor are important quantities that provide information about the quality of the extracted quantum light. On resonance and for optimal dipole alignment, we define the cavity-emitter cooperativity as $C \equiv 4g^2/(\kappa\Gamma_0)$, where g is the vacuum Rabi frequency, κ the cavity energy-decay rate, and Γ_0 the free-space spontaneous-emission rate. The cavity-enhanced decay rate is then $\Gamma = \Gamma_0(1+C)$, i.e. the Purcell enhancement $\mathcal{F} \equiv \Gamma/\Gamma_0 = 1+C$. The fraction of emission funneled into the bright cavity mode (the β -factor) is

$$\beta_{\text{cav}} = \frac{C}{\mathcal{F}} = \frac{C}{1+C} = \frac{\mathcal{F}-1}{\mathcal{F}}. \quad (26)$$

Including dissipative loss via the quantum efficiency $QE \equiv \Gamma_{\text{rad}}/(\Gamma_{\text{rad}} + \Gamma_{\text{loss}})$, the far-field (device-relevant) branching ratio is

$$\beta_{\text{ext}} = \beta_{\text{cav}} \times QE \simeq QE \quad (C \gg 1). \quad (27)$$

Thus, approaching deterministic single-photon emission corresponds to $\beta_{\text{ext}} \rightarrow 1$; for symmetric two-photon emission, the pair-in-mode probability scales as $\beta_{\text{pair}} \simeq \beta_{\text{ext}}^2$. Using high-mobility graphene, for the mid-IR cavity design, we have $\beta_{\text{ext}} = QE = 0.95$ and for the telecommunications cavity design we have $\beta_{\text{ext}} = QE = 0.89$ for high-mobility graphene. Thus, for the entangled-photon emission in the case of high-mobility graphene at $\lambda = 1.55 \mu\text{m}$, we obtain $\beta_{\text{pair}} \simeq \beta_{\text{ext}}^2 = QE^2 = 0.79$.

II. Conclusion

Here we have demonstrated that metallic nanoparticles on an hBN/graphene/SU-8 heterostructure can produce a large Purcell enhancement effect via coupling of SPEs to the supported AGP eigenmodes in the cavity of the heterostructure. We showed that enhancement factors of up to eight orders of magnitude are possible when using hBN thicknesses of 1 nm. We showed that the frequency of these AGPs is determined by the geometry of the cavity, specifically the thickness of the hBN layer and the number of graphene layers intercalated with FeCl_3 . Importantly, the AGP frequency can also be tuned via a gate voltage applied to the graphene layer which varies the graphene's Fermi energy. This allows for the AGP frequency to be varied with respect to time, enabling the Purcell enhancement to be effectively switched on and off. The resulting Purcell enhancement factors are on the order of several million in the mid IR, with radiative enhancements exceeding 10^6 . This enhancement enables high quantum yield for single-photon emission and makes electric quadrupole and two-photon spontaneous emission (2PSE) experimentally accessible. Quadrupole transitions are particularly compelling, as they allow the emitted photons to carry orbital angular momentum. This additional degree of freedom opens new avenues for encoding information, offering significant advantages for quantum communication technologies. By changing the values of E_F , C_S , and h we can tune the AGP to wavelengths of interest in telecommunications at the expense of a reduction in the enhancement rate. For example, at 1550 nm we demonstrate a Purcell enhancement of 1.76×10^4 for dipole transitions, 1.19×10^7 for quadrupole transitions, and 3.1×10^8 for 2PSE. Remarkably, we show that using high-mobility graphene it is possible to reach quantum efficiencies of 95% and 89% in the mid-IR and near-IR, respectively. In addition, we obtain a quantum efficiency of 79% for entangled-photon emission with high-mobility graphene at $\lambda = 1.55 \mu\text{m}$. These large Purcell enhancement factors and the high quantum efficiencies at mid-IR and near-IR wavelengths make the metamaterials based on Ag nanoparticles on dielectric/graphene a promising platform for the development of single-photon and entangled-photon sources for use in telecommunications. We also showed that the Purcell enhancement of forbidden transitions can be greatly increased. This enhancement allows for transitions that were previously not detectable by experiment, to be utilized in applications related to quantum information science and engineering.

III. Methods

Graphene Material Parameters

The finite-difference time-domain (FDTD) simulations were performed using the commercial Ansys Lumerical FDTD software. The graphene layer is modeled as a 2D plane with a total conductivity defined as the optical conductivity of graphene with linear dispersion, giving rise to the intraband

optical conductivity^{113–116}

$$\sigma_{\text{intra}}(\omega) = \frac{e^2}{\pi\hbar^2} \frac{2k_B T}{\tau^{-1} - i\omega} \ln \left[2 \cosh \left(\frac{\varepsilon_F}{2k_B T} \right) \right], \quad (28)$$

which in the case of $\varepsilon_F \gg k_B T$ is reduced to

$$\sigma_{\text{intra}}(\omega) = \frac{e^2}{\pi\hbar^2} \frac{\varepsilon_F}{\tau^{-1} - i\omega} = \frac{2\varepsilon_m \omega_p^2}{\pi\hbar^2(\tau^{-1} - i\omega)}, \quad (29)$$

where τ is determined by impurity scattering and electron-phonon interaction $\tau^{-1} = \tau_{\text{imp}}^{-1} + \tau_{e-ph}^{-1}$. Using the mobility μ of the graphene sheet, it can be presented in the form $\tau^{-1} = ev_F^2/(\mu E_F)$, where $v_F = 10^6$ m/s is the Fermi velocity in graphene. $\omega_p = \sqrt{e^2 E_F / 2\varepsilon_m}$ is the bulk graphene plasma frequency. We use a graphene mobility of 2000 cm²V⁻¹s⁻¹. Since the graphene sheets are electronically decoupled from each other by the insulating FeCl₃ layers, the optical conductivity of multilayer graphene (MLG) intercalated with FeCl₃ is given by¹¹⁷

$$\sigma_{\text{intra}}^{\text{MLG-FeCl}_3}(\omega) = N \frac{e^2}{\pi\hbar^2} \frac{E_F}{\tau^{-1} - i\omega}, \quad (30)$$

where N is the number of graphene layers. This formula is only valid for excitation energies below the band gap $E_g = 1$ eV of FeCl₃. Since we study AGP resonances at energies between 0.18 eV ($\lambda = 7.0$ μm) and 1.24 eV ($\lambda = 1.0$ μm), we can safely neglect the optical phonons in FeCl₃ at 2.7 meV and 7 meV.

To model multiple layers of graphene intercalated with FeCl₃, we utilize the conductivity scaling variable in the Lumerical FDTD software. The validity of this approach to model multi-layer graphene is discussed later. The mesh size is set within the dielectric layer, consisting of hBN or hBN with WS₂, to be 1 nm in the x and y directions and 0.5 nm in the z direction. The auto shutoff level is set to 10⁻⁷ and the simulation time to 40000 μs.

The following quantities are useful to understand the methods of extracting the Purcell enhancement factors, the spontaneous decay rates, the normalized spontaneous decay rates, and the quantum efficiency from FDTD simulations.

Purcell Enhancement Factor and Spontaneous Decay Rates

The emission rate of a quantum emitter, Γ_{emi} , in the presence of an antenna is determined by the excitation rate, Γ_{exc} , and the quantum efficiency, QE . Assuming these effects are uncorrelated, i.e.

$$\Gamma_{\text{emi}} = \Gamma_{\text{exc}} \cdot QE. \quad (31)$$

In a homogeneous medium (denoted by superscript ‘0’), we have

$$\frac{\Gamma_{\text{emi}}}{\Gamma_{\text{emi}}^0} = \frac{\Gamma_{\text{exc}}}{\Gamma_{\text{exc}}^0} \frac{QE}{QE^0}. \quad (32)$$

The enhancement of the excitation rate is given by

$$\frac{\Gamma_{\text{exc}}}{\Gamma_{\text{exc}}^0} = \frac{|\mathbf{E}|^2}{|\mathbf{E}^0|^2}. \quad (33)$$

The quantum efficiency, QE , is defined as the ratio between radiative decay rates and total decay rates, i.e.

$$QE = \frac{\Gamma_{\text{rad}}}{\Gamma_{\text{rad}} + \Gamma_{\text{nr}} + \Gamma_{\text{loss}}}. \quad (34)$$

Normalized Spontaneous Decay Rates

Absolute decay rates Γ_{rad} , Γ_{rad}^0 , Γ_{loss} cannot be directly calculated, but their normalized forms can be used by using the ratio

$$\frac{\Gamma_{\text{dip}}}{\Gamma_{\text{rad}}^0} = \frac{P_{\text{dip}}}{P_{\text{rad}}^0}. \quad (35)$$

The Purcell enhancement factor is

$$\mathcal{F} = \frac{\Gamma_{\text{dip}}}{\Gamma_{\text{rad}}^0}. \quad (36)$$

The normalized spontaneous decay rates are

$$\frac{\Gamma_{\text{rad}}}{\Gamma_{\text{rad}}^0} = \frac{P_{\text{rad}}}{P_{\text{rad}}^0}, \quad \frac{\Gamma_{\text{loss}}}{\Gamma_{\text{rad}}^0} = \frac{P_{\text{abs}}}{P_{\text{rad}}^0}. \quad (37)$$

Quantum Efficiency

For a high intrinsic quantum efficiency (assuming $QE^0 = 1$ and $\Gamma_{\text{nr}}^0 = 0$) we have

$$\frac{QE}{QE^0} = QE = \frac{\Gamma_{\text{rad}}}{\Gamma_{\text{rad}} + \Gamma_{\text{loss}}}. \quad (38)$$

This is the ratio of power radiated to the sum of radiated and absorbed power. The QE of the device is plotted for both wavelengths of interest in Fig. 8.

Acknowledgment

M.A.K., M.N.L., and D.R.E. acknowledge support by the Air Force Office of Scientific Research (AFOSR) under award no. FA9550-23-1-0472.

¹Aharonovich, I.; Englund, D.; Toth, M. Solid-state single-photon emitters. *Nature Photonics* **2016**, *10*, 631–641.

²Senellart, P.; Solomon, G.; White, A. High-performance semiconductor quantum-dot single-photon sources. *Nature Nanotechnology* **2017**, *12*, 1026–1039.

³Aharonovich, I.; Neu, E. Diamond Nanophotonics. *Advanced Optical Materials* **2014**, *2*, 911–928.

⁴Tran, T. T.; Bray, K.; Ford, M. J.; Toth, M.; Aharonovich, I. Quantum emission from hexagonal boron nitride monolayers. *Nature Nanotechnology* **2015**, *11*, 37–41.

⁵Tonndorf, P.; Schmidt, R.; Schneider, R.; Kern, J.; Buscema, M.; Steele, G. A.; Castellanos-Gomez, A.; van der Zant, H. S. J.; de Vasconcellos, S. M.; Bratschitsch, R. Single-photon emission from localized excitons in an atomically thin semiconductor. *Optica* **2015**, *2*, 347–352.

⁶Srivastava, A.; Sidler, M.; Allain, A. V.; Lembke, D. S.; Kis, A.; Imamoglu, A. Optically active quantum dots in monolayer WSe₂. *Nature Nanotechnology* **2015**, *10*, 491–496.

⁷Chakraborty, C.; Kinnischitzke, L.; Goodfellow, K. M.; Beams, R.; Vamivakas, A. N. Voltage-controlled quantum light from an atomically thin semiconductor. *Nature Nanotechnology* **2015**, *10*, 507–U38.

⁸Koperski, M.; Nogajewski, K.; Arora, A.; Cherkez, V.; Mallet, P.; Veuillen, J. Y.; Marcus, J.; Kossacki, P.; Potemski, M. Single photon emitters in exfoliated WSe₂ structures. *Nature Nanotechnology* **2015**, *10*, 503–506.

⁹He, Y.-M.; Clark, G.; Schaibley, J. R.; He, Y.; Chen, M.-C.; Wei, Y.-J.; Ding, X.; Zhang, Q.; Yao, W.; Xu, X.; et al. Single Quantum emitters in monolayer semiconductors. *Nature Nanotechnology* **2015**, *10*, 497–502.

¹⁰Dass, C. K.; Khan, M. A.; Clark, G.; Simon, J. A.; Gibson, R.; Mou, S.; Xu, X.; Leuenberger, M. N.; Hendrickson, J. R. Ultra-Long Lifetimes of Single Quantum Emitters in Monolayer WSe₂/hBN Heterostructures. *Advanced Quantum Technologies* **2019**, *2*, 1900022.

¹¹Tonndorf, P.; Schwarz, S.; Kern, J.; Niehues, I.; Pozo-Zamudio, O. D.; Dmitriev, A. I.; Bakhtinov, A. P.; Borisenko, D. N.; Kolesnikov, N. N.; Tartakovskii, A. I.; de Vasconcellos, S. M.; Bratschitsch, R. Single-photon emitters in GaSe. *2D Materials* **2017**, *4*, 021010.

¹²Redjem, W.; Durand, A.; Herzig, T.; Benali, A.; Pezzagna, S.; Meijer, J.; Kuznetsov, A. Y.; Nguyen, H. S.; Cueff, S.; Gérard, J.-M.; Robert-Philip, I.; Abbarchi, M.; Jacques, V.; Cassabois, G.; Dréau, A. Single artificial atoms in silicon emitting at telecom wavelengths. *Nature Electronics* **2020**, *3*, 738–743.

¹³Durand, A.; Baron, Y.; Redjem, W.; Herzig, T.; Benali, A.; Pezzagna, S.; Meijer, J.; Kuznetsov, A. Y.; Gérard, J.-M.; Robert-Philip, I.; Abbarchi, M.; Jacques, V.; Cassabois, G.; Dréau, A. Broad Diversity of Near-Infrared Single-Photon Emitters in Silicon. *Physical Review Letters* **2021**, *126*, 083602.

¹⁴Hollenbach, M.; Klingner, N.; Jagtap, N. S.; et al. Wafer-scale nanofabrication of telecom single-photon emitters in silicon. *Nature Communications* **2022**, *13*, 7692.

¹⁵Ivanov, V.; et al. Effect of localization on photoluminescence and zero-field splitting in silicon color centers. *Physical Review B* **2022**, *106*, 134107.

¹⁶Durand, A.; et al. Genuine and faux single centers in carbon-implanted silicon. *Physical Review B* **2024**, *110*, L020102.

¹⁷Durand, A.; et al. Hopping of the Center-of-Mass of Single G Centers in Silicon-on-Insulator. *Physical Review X* **2024**, *14*, 041071.

¹⁸Prabhu, M.; Errando-Herranz, C.; De Santis, L.; Christen, I.; Chen, C.; Gerlach, C.; Englund, D. R. Individually addressable and spectrally programmable artificial atoms in silicon photonics. *Nature Communications* **2023**, *14*, 2555.

¹⁹Larocque, H.; Buyukkaya, M. A.; Errando-Herranz, C.; Papon, C.; Tao, M.; Carolan, J.; Lee, C.-M.; Richardson, C. J. K.; Leake, G. L.; Coleman, D. J.; Fanto, M. L.; Waks, E.; Englund, D. Tunable quantum emitters on large-scale foundry silicon photonics. *Nature Communications* **2024**, *15*, 5781.

²⁰Komza, L.; Samutpraphoot, P.; Odeh, M.; Tang, Y.-L.; Mathew, M.; Chang, J.; Song, H.; Kim, M.-K.; Xiong, Y.; Hautier, G.; Sipahigil, A. A. Indistinguishable photons from an artificial atom in silicon photonics. *Nature Communications* **2024**, *15*, 51265.

²¹Redjem, W.; Zhiyenbayev, Y.; Qarony, W.; et al. All-silicon quantum light source by embedding an atomic emissive center in a nanophotonic cavity. *Nature Communications* **2023**, *14*, 3321.

²²Lee, C.-M.; Islam, F.; Harper, S.; Buyukkaya, M. A.; Higginbottom, D.; Simmons, S.; Waks, E. High-Efficiency Single Photon Emission from a Silicon T-Center in a Nanobeam. *ACS Photonics* **2023**, *10*, 3844–3849.

²³Islam, F.; Lee, C.-M.; Harper, S.; Rahaman, M. H.; Zhao, Y.; Vij, N. K.; Waks, E. Cavity-Enhanced Emission from a Silicon T Center. *Nano Letters* **2024**, *24*, 319–325.

²⁴Johnston, A.; Felix-Rendon, U.; Wong, Y.-E.; Chen, S. Cavity-coupled telecom atomic source in silicon. *Nature Communications* **2024**, *15*, 2350.

²⁵Gritsch, A.; Ulanowski, A.; Reiserer, A. Purcell enhancement of single-photon emitters in silicon. *Optica* **2023**, *10*, 783–789.

²⁶Saggio, V.; et al. Cavity-enhanced single artificial atoms in silicon. *Nature Communications* **2024**, *15*, 4663.

²⁷Gritsch, A.; Ulanowski, A.; Pforr, J.; Reiserer, A. Narrow Optical Transitions in Erbium-Implanted Silicon with Controlled Lattice Sites. *Physical Review X* **2022**, *12*, 041009.

²⁸Gritsch, A.; Ulanowski, A.; Pforr, J.; Reiserer, A.; collaborators Optical single-shot readout of spin qubits in silicon. *Nature Communications* **2025**, *16*, 64.

²⁹Berkman, I. R.; collaborators Long optical and electron spin coherence times for erbium ions in silicon. *npj Quantum Information* **2025**, *11*, 66.

³⁰Yin, C.; Rancic, M.; de Boo, G. G.; Stavrias, N.; McCallum, J. C.; Sellars, M. J.; Rogge, S. Optical addressing of an individual erbium ion in silicon. *Nature* **2013**, *497*, 91–94.

³¹Rinner, S.; Ulanowski, A.; Schönfuss, D.; Reiserer, A. Erbium emitters in commercially fabricated nanophotonic silicon devices. *Nanophotonics* **2023**, *12*, 3081–3092.

³²Dibos, A. M.; Raha, M.; Phenicie, C. M.; Ourari, S.; Awschalom, D. D.; Thompson, J. D.; de Leon, N. P.; coauthors Purcell Enhancement of Erbium Ions in TiO₂ on Silicon Nanocavities. *Nano Letters* **2022**, *22*, 6418–6425.

³³Xu, Z.; colleagues Isolation of individual Er quantum emitters in anatase TiO₂ thin films on silicon. *Applied Physics Letters* **2024**, *125*, 084001.

³⁴Singh, M. K.; Grant, G. D.; Wolfowicz, G.; others Optical and microstructural studies of erbium-doped TiO₂ thin films on silicon, SrTiO₃, and sapphire. *Journal of Applied Physics* **2024**, *136*, 124402.

³⁵Ourari, S.; Dusanowski, L.; Horvath, S. P.; Uysal, M. T.; Phenicie, C. M.; Stevenson, P.; Raha, M.; Chen, S.; Cava, R. J.; de Leon, N. P.; Thompson, J. D. Indistinguishable telecom band photons from a single Er ion in the solid state. *Nature* **2023**, *620*, 977–981.

³⁶Uysal, M. T.; Ourari, S.; colleagues Spin–Photon Entanglement of a Single Ion in the Telecom Band. *Physical Review X* **2025**, *15*, 011071.

³⁷Yang, L.; Ourari, S.; Ourjoumtsev, A.; Pépin, N.; others Controlling single rare-earth-ion emission in an electro-optically tunable cavity. *Nature Communications* **2023**, *14*, 3137.

³⁸Yang, L.; Ourjoumtsev, A.; Rancic, M.; Sellars, M. J.; Thompson, J. D. Integration of Er³⁺:Y₂SiO₅ with thin-film lithium niobate by flip-chip bonding. *Optics Express* **2021**, *29*, 15497–15506.

³⁹Huang, J.-Y.; Liang, P.-J.; Zheng, L.; Li, P.-Y.; Ma, Y.-Z.; Liu, D.-C.; Xie, J.-H.; Zhou, Z.-Q.; Li, C.-F.; Guo, G.-C. Stark Tuning of Telecom Single-Photon Emitters Based on a Single Er³⁺. *Chinese Physics Letters* **2023**, *40*, 070301.

⁴⁰Branny, A.; Kumar, S.; Proux, R.; Gerardot, B. D. Deterministic strain-induced arrays of quantum emitters in a two-dimensional semiconductor. *Nature Communications* **2017**, *8*, 15053.

⁴¹Paralikis, A.; Piccinini, C.; Madigawa, A. A.; Metuh, P.; Vannucci, L.; GregerSEN, N.; Munkhbat, B. Tailoring polarization in WSe₂ quantum emitters through deterministic strain engineering. *npj 2D Materials and Applications* **2024**, *8*, 59.

⁴²Luo, Y.; Shepard, G. D.; Ardelean, J. V.; Rhodes, D. A.; Kim, B.; Barakat, K.; Hone, J. C.; Strauf, S. Deterministic coupling of site-controlled quantum emitters in monolayer WSe₂ to plasmonic nanocavities. *Nature Nanotechnology* **2018**, *13*, 1137–1142.

⁴³So, J.-P.; Kim, H.-R.; Baek, H.; Jeong, K.-Y.; Lee, H.-C.; Huh, W.; Kim, Y. S.; Watanabe, K.; Taniguchi, T.; Kim, J.; Lee, C.-H.; Park, H.-G. Electrically driven strain-induced deterministic single-photon emitters in a van der Waals heterostructure. *Science Advances* **2021**, *7*, eabj3176.

⁴⁴Guo, S.; Germanis, S.; Taniguchi, T.; Watanabe, K.; Withers, F.; Luxmoore, I. J. Electrically Driven Site-Controlled Single Photon Source Based on a WSe₂ Vertical Tunneling LED. *ACS Photonics* **2023**, *10*, 2549–2555.

⁴⁵Howarth, J.; Vaklinova, K.; Grzeszczyk, M.; Baldi, G.; Hague, L.; Potemski, M.; Novoselov, K. S.; Kozikov, A.; Koperski, M. Electroluminescent vertical tunneling junctions based on WSe₂ monolayer quantum emitter arrays: Exploring tunability with electric and magnetic fields. *Proceedings of the National Academy of Sciences* **2024**, *121*, e2401757121.

⁴⁶Tran, T. T.; Bray, K.; Ford, M. J.; Toth, M.; Aharonovich, I. Quantum emission from hexagonal boron nitride monolayers. *Nature Nanotechnology* **2016**, *11*, 37–41.

⁴⁷Bourrellier, R.; Meuret, S.; Tararan, A.; Stéphan, O.; Kociak, M.; Tizei, L. H. G.; Zobelli, A. Bright UV Single Photon Emission at Point Defects in h-BN. *Nano Letters* **2016**, *16*, 4317–4321.

⁴⁸Grosso, G.; Moon, H.; Lienhard, B.; Ali, S.; Efetov, D. K.; Furchi, M. M.; Jarillo-Herrero, P.; Ford, M. J.; Aharonovich, I.; Englund, D. Tunable and high-purity room-temperature single-photon emission from atomic defects in hexagonal boron nitride. *Nature Communications* **2017**, *8*, 705.

⁴⁹Shotan, Z.; Jayakumar, H.; Considine, C. R.; Mackoit, M.; Fedder, H.; Wrachtrup, J.; Alkauskas, A.; Doherty, M. W.; Menon, V. M.; Meriles, C. A. Photoinduced Modification of Single-Photon Emitters in Hexagonal Boron Nitride. *ACS Photonics* **2016**, *3*, 2490–2496.

⁵⁰Noh, G.; Choi, D.; Kim, J.-H.; Im, D.-G.; Kim, Y.-H.; Seo, H.; Lee, J. Stark Tuning of Single-Photon Emitters in Hexagonal Boron Nitride. *Nano Letters* **2018**, *18*, 4710–4715.

⁵¹Proscia, N. V.; Shotan, Z.; Jayakumar, H.; Reddy, P.; Dollar, M.; Alkauskas, A.; Doherty, M.; Meriles, C. A.; Menon, V. M. Near-deterministic activation of room-temperature quantum emitters in hexagonal boron nitride. *Optica* **2018**, *5*, 1128–1134.

⁵²Patel, R. N.; Hopper, D. A.; Gusdorf, J. A.; Turiansky, M. E.; Huang, T.-Y.; Fishman, R. E. K.; Porat, B.; Van de Walle, C. G.; Bassett, L. C. Probing the Optical Dynamics of Quantum Emitters in Hexagonal Boron Nitride. *PRX Quantum* **2022**, *3*, 030331.

⁵³Sajid, A.; Ford, M. J.; Reimers, J. R. Single-photon emitters in hexagonal boron nitride: a review of progress. *Reports on Progress in Physics* **2020**, *83*, 044501.

⁵⁴Aharonovich, I.; Toth, M. Quantum emitters in hexagonal boron nitride. *Nano Letters* **2022**, *22*, 4425–4435.

⁵⁵Prasad, M. K.; Taverne, M. P. C.; Huang, C.-C.; Mar, J. D.; Ho, Y.-L. D. Hexagonal Boron Nitride Based Photonic Quantum Technologies. *Materials* **2024**, *17*, 4122.

⁵⁶Mendelson, N.; Doherty, M.; Toth, M.; Aharonovich, I.; Tran, T. T. Strain-Induced Modification of the Optical Characteristics of Quantum Emitters in Hexagonal Boron Nitride. *Advanced Materials* **2020**, *32*, e1908316.

⁵⁷Im, S.; Moon, S.; Kim, J.; Song, J.; Ji, C.; Kim, J. K. Quantum Emitters Based on Hexagonal Boron Nitride for Next-Generation Quantum Technology. *Progress in Quantum Electronics* **2025**, *92*, 100511.

⁵⁸Li, S.; Pershin, A.; Thiering, G.; Udvarhelyi, P.; Gali, A. Ultraviolet Quantum Emitters in Hexagonal Boron Nitride from Carbon Clusters. *The Journal of Physical Chemistry Letters* **2022**, *13*, 3150–3157.

⁵⁹Chen, Y.; Chen, H.; Bogdanov, N.; Yu, K.; Alavi, A.; Wang, E.; Chen, J. Towards an accurate electronic structure of single photon emitters in hexagonal boron nitride. *Physical Review Research* **2025**, *7*, L012079.

⁶⁰Baek, H.; Brotons-Gisbert, M.; Koong, Z. X.; Campbell, A.; Rambach, M.; Watanabe, K.; Taniguchi, T.; Gerardot, B. D. Highly energy-tunable quantum light from moiré-trapped excitons. *Science Advances* **2020**, *6*, eaba8526.

⁶¹Qian, C.; Troue, M.; Figueiredo, J.; Soubelet, P.; Villaflaño, V.; Beierlein, J.; Klembt, S.; Stier, A. V.; Höfling, S.; Holleitner, A. W.; Finley, J. J. Lasing of moiré trapped MoSe₂/WSe₂ interlayer excitons coupled to a nanocavity. *Science Advances* **2024**, *10*, eadk6359.

⁶²Wang, H.; Kim, H.; Dong, D.; Shinokita, K.; Watanabe, K.; Taniguchi, T.; Matsuda, K. Quantum coherence and interference of a single moiré exciton in nano-fabricated twisted monolayer semiconductor heterobilayers. *Nature Communications* **2024**, *15*, 4905.

⁶³Alexeev, E. M. et al. Nature of Long-Lived Moiré Interlayer Excitons in Electrically Tunable MoS₂/MoSe₂ Heterobilayers. *Nano Letters* **2024**, *24*, 11232–11238.

⁶⁴Cai, H. et al. Interlayer donor–acceptor pair excitons in MoSe₂/WSe₂ moiré heterobilayer. *Nature Communications* **2023**, *14*, 5766.

⁶⁵Förg, M.; Baimuratov, A. S.; Kruchinin, S. Y.; Vovk, I. A.; Scherzer, J.; Förste, J.; Funk, V.; Watanabe, K.; Taniguchi, T.; Högele, A. Moiré excitons in MoSe₂–WSe₂ heterobilayers and heterotrilayers. *Nature Communications* **2021**, *12*, 1656.

⁶⁶Brotons-Gisbert, M.; Baek, H.; Campbell, A.; Watanabe, K.; Taniguchi, T.; Gerardot, B. D. Moiré-Trapped Interlayer Triions in a Charge-Tunable WSe₂/MoSe₂ Heterobilayer. *Physical Review X* **2021**, *11*, 031033.

⁶⁷Lin, Q.; Fang, H.; Kalaboukhov, A.; Liu, Y.; Zhang, Y.; Fischer, M.; Li, J.; Hagel, J.; Brem, S.; Malic, E.; Stenger, N.; Sun, Z.; Wubs, M.; Xiao, S. Moiré-engineered light–matter interactions in MoS₂/WSe₂ heterobilayers at room temperature. *Nature Communications* **2024**, *15*, 8762.

⁶⁸Zhang, C.; Guo, Z.; He, D.; Yang, Y.; Li, S.; Zou, K.; Wang, J.; Wang, Y.; Zhang, X. Research Progress of Single-Photon Emitters Based on Two-Dimensional Materials. *Micromachines* **2024**, *15*, 617.

⁶⁹Bonneville, D. B.; Osornio-Martinez, C. E.; Dijkstra, M.; García-Blanco, S. M. High on-chip gain spiral Al₂O₃:Er³⁺ waveguide amplifiers. *Opt. Express* **2024**, *32*, 15527–15536.

⁷⁰Worhoff, K.; Bradley, J. D. B.; Ay, F.; Geskus, D.; Blauwendraat, T. P.; Pollnau, M. Reliable Low-Cost Fabrication of Low-Loss Al₂O₃:Er³⁺ Waveguides With 5.4-dB Optical Gain. *IEEE Journal of Quantum Electronics* **2009**, *45*, 454–461.

⁷¹Bai, G.; Yuan, S.; Zhao, Y.; Yang, Z.; Choi, S. Y.; Chai, Y.; Yu, S. F.; Lau, S. P.; Hao, J. 2D Layered Materials of Rare-Earth Er-Doped MoS₂ with NIR-to-NIR Down- and Up-Conversion Photoluminescence. *Advanced Materials* **2016**, *28*, 7472–7477.

⁷²Huang, Y.; Zhao, Y.; Liu, Y.; Ye, R.; Chen, L.; Bai, G.; Xu, S. Erbium-doped tungsten selenide nanosheets with near-infrared II emission and photothermal conversion. *Chemical Engineering Journal* **2021**, *411*, 128610.

⁷³Cholsuk, C.; Suwanna, S.; Vogl, T. Tailoring the Emission Wavelength of Color Centers in Hexagonal Boron Nitride for Quantum Applications. *Nanomaterials* **2022**, *12*.

⁷⁴Koppens, F. H.; Chang, D. E.; García de Abajo, F. J. Graphene plasmonics: A platform for strong light–matter interactions. *Nano Letters* **2011**, *11*, 3370–3377.

⁷⁵Sanders, S.; May, A.; Alabastri, A.; Manjavacas, A. Extraordinary enhancement of quadrupolar transitions using nanostructured graphene. *ACS Photonics* **2018**, *5*, 3282–3290.

⁷⁶Manjavacas, A.; Nordlander, P.; García de Abajo, F. J. Plasmon blockade in nanostructured graphene. *ACS Nano* **2012**, *6*, 1724–1731.

⁷⁷Cox, J. D.; Singh, M. R.; Gumbs, G.; Anton, M. A.; Carreno, F. Dipole–dipole interaction between a quantum dot and a graphene nanodisk. *Physical Review B* **2012**, *86*.

⁷⁸Karanikolas, V.; Tozman, P.; Paspalakis, E. Light-matter interaction of a quantum emitter near a half-space graphene nanostructure. *Physical Review B* **2019**, *100*.

⁷⁹Rosolen, G.; Maes, B. Strong multipolar transition enhancement with graphene nanoislands. *APL Photonics* **2021**, *6*, 086103.

⁸⁰Mendelson, N.; Ritika, R.; Kianinia, M.; Scott, J.; Kim, S.; Fröch, J. E.; Gazzana, C.; Westerhausen, M.; Xiao, L.; Mohajerani, S. S.; Strauf, S.; Toth, M.; Aharonovich, I.; Xu, Z.-Q. Coupling Spin Defects in a Layered Material to Nanoscale Plasmonic Cavities. *Advanced Materials* **2022**, *34*, 2106046.

⁸¹Xu, X. et al. Greatly Enhanced Emission from Spin Defects in Hexagonal Boron Nitride Enabled by a Low-Loss Plasmonic Nanocavity. *Nano Letters* **2023**, *23*, 25–33.

⁸²Dowran, M.; Butler, A.; Lamichhane, S.; Erickson, A.; Kilic, U.; Liou, S.-H.; Argyropoulos, C.; Laraoui, A. Plasmon Enhanced Quantum Properties of Single Photon Emitters with Hybrid Hexagonal Boron Nitride Silver Nanocube Systems. *Advanced Optical Materials* **2023**, *11*, 2300392.

⁸³Gottscholl, A.; Kianinia, M.; Soltamov, V.; Orlinskii, S.; Mamin, G.; Bradac, C.; Kasper, C.; Krambrock, K.; Sperlich, A.; Toth, M.; Aharonovich, I.; Dyakonov, V. Initialization and read-out of intrinsic spin defects in a van der Waals crystal at room temperature. *Nature Materials* **2020**, *19*, 540–545.

⁸⁴Gottscholl, A.; Diez, M.; Soltamov, V.; Kasper, C.; Sperlich, A.; Kianinia, M.; Bradac, C.; Aharonovich, I.; Dyakonov, V. Room temperature coherent control of spin defects in hexagonal boron nitride. *Science Advances* **2021**, *7*, eabf3630.

⁸⁵Wolfowicz, G.; Heremans, F. J.; Anderson, C. P.; Kanai, S.; Seo, H.; Gali, A.; Galli, G.; Awschalom, D. D. Quantum guidelines for solid-state spin defects. *Nature Reviews Materials* **2021**, *6*, 906–925.

⁸⁶Awschalom, D. D.; Hanson, R.; Wrachtrup, J.; Zhou, B. B. Quantum technologies with optically interfaced solid-state spins. *Nature Photonics* **2018**, *12*, 516–527.

⁸⁷Epstein, I.; Alcaraz, D.; Huang, Z.; Pusapati, V.-V.; Hugonin, J.-P.; Kumar, A.; Deputy, X. M.; Khodkov, T.; Rappoport, T. G.; Hong, J.-Y.; Peres, N. M. R.; Kong, J.; Smith, D. R.; Koppens, F. H. L. Far-field excitation of single graphene plasmon cavities with ultracompressed mode volumes. *Science* **2020**, *368*, 1219–1223.

⁸⁸Craft, J. D.; Shabbir, M. W.; Englund, D. R.; Osgood, R. M. I.; Leuenberger, M. N. Spectrally Selective Thermal Emission from Graphene Decorated with Metallic Nanoparticles. *J. Phys. Chem. C* **2023**, *127*, 8186–8194.

⁸⁹Tafur, S.; Leuenberger, M. N. Computational model of single-photon near-field emission. Quantum Information and Computation IX. 2011; p 805704.

⁹⁰Tafur, S.; Leuenberger, M. N. Spontaneous Creation of Photonic States in Quantum Dots. *Rev. Nanosci. Nanotechnol.* **2012**, *1*, 152–161.

⁹¹Tafur, S. Computational Study Of The Near Field Spontaneous Creation Of Photonic States Coupled To Few Level Systems. Doctoral dissertation, University of Central Florida, Orlando, FL, 2011; Electronic Theses and Dissertations, no. 1799. Identifier: CFE0003881.

⁹²Meystre, P.; Sargent III, M. *Elements of Quantum Optics*, 4th edition; Springer, 2007.

⁹³Purcell, E. M. Spontaneous emission probabilities at radio frequencies. *Phys. Rev.* **1946**, *69*, 681.

⁹⁴Zhan, D.; Sun, L.; Ni, Z. H.; Liu, L.; Fan, X. F.; Wang, Y.; Yu, T.; Lam, Y. M.; Huang, W.; Shen, Z. X. FeCl₃-Based Few-Layer Graphene Intercalation Compounds: Single Linear Dispersion Electronic Band Structure and Strong Charge Transfer Doping. *Advanced Functional Materials* **2010**, *20*, 3504–3509.

⁹⁵Gonçalves, P.; Christensen, T.; Peres, N. M.; Jauho, A.-P.; Epstein, I.; Koppen, F. H.; Soljačić, M.; Mortensen, N. A. Quantum surface-response of metals revealed by acoustic graphene plasmons. *Nature Communications* **2021**, *12*, 3271.

⁹⁶Zomer, P. J.; Dash, S. P.; Tombros, N.; van Wees, B. J. A transfer technique for high mobility graphene devices on commercially available hexagonal boron nitride. *Applied Physics Letters* **2011**, *99*, 232104.

⁹⁷Martini, L.; Mišekis, V.; Esteban, D.; Azpeitia, J.; Pezzini, S.; Paletti, P.; Ochapski, M. W.; Convertino, D.; Hernandez, M. G.; Jimenez, I.; Coletti, C. Scalable High-Mobility Graphene/hBN Heterostructures. *ACS Applied Materials & Interfaces* **2023**, *15*, 37794–37801.

⁹⁸Rivera, N.; Kaminer, I.; Zhen, B.; Joannopoulos, J. D.; Soljačić, M. Shrinking light to allow forbidden transitions on the atomic scale. *Science* **2016**, *353*, 263–269.

⁹⁹Nordlander, P.; Oubre, C.; Prodan, E.; Li, K.; Stockman, M. I. Plasmon Hybridization in Nanoparticle Dimers. *Nano Letters* **2004**, *4*, 899–903.

¹⁰⁰Bai, G.; Yang, Z.; Lin, H.; Jie, W.; Hao, J. Lanthanide Yb/Er co-doped semiconductor layered WSe₂ nanosheets with near-infrared luminescence at telecommunication wavelengths. *Nanoscale* **2018**, *10*, 9261–9267.

¹⁰¹Wang, L.; Song, E.; Zhang, S.; Hou, X.; Ji, X.; Zhang, Q. Enhanced Visible-Light Response of Ultrathin Er-Doped MoS₂ Nanosheets through a Wet-Chemical Method. *The Journal of Physical Chemistry C* **2023**, *127*, 1407–1414.

¹⁰²Khan, M.; Leuenberger, M. N. Ab initio calculations for electronic and optical properties of Er₂ defects in single-layer tungsten disulfide. *Journal of Applied Physics* **2021**, *130*, 115104.

¹⁰³Quantum ATK 2022. *Synopsys Quantum ATK* **2022**.

¹⁰⁴Khan, M. A.; Craft, J. D.; Paudel, H. P.; Duan, Y.; Englund, D. R.; Leuenberger, M. N. Er₃:Al₂O₃ for Telecom-Band Photonics: Electronic Structure and Optical Properties. *arXiv preprint arXiv:2509.18409* **2025**,

¹⁰⁵Judd, B. R. Optical Absorption Intensities of Rare-Earth Ions. *Phys. Rev.* **1962**, *127*, 750–761.

¹⁰⁶Ofelt, G. S. Intensities of Crystal Spectra of Rare-Earth Ions. *The Journal of Chemical Physics* **1962**, *37*, 511–520.

¹⁰⁷Dodson, C. M.; Zia, R. Magnetic dipole and electric quadrupole transitions in the trivalent lanthanide series: Calculated emission rates and oscillator strengths. *Phys. Rev. B* **2012**, *86*, 125102.

¹⁰⁸Erhard, M.; Fickler, R.; Krenn, M.; Zeilinger, A. Twisted photons: new quantum perspectives in high dimensions. *Light: Science & Applications* **2018**, *7*, 17146–17146.

¹⁰⁹Yao, A. M.; Padgett, M. J. Orbital angular momentum: origins, behavior and applications. *Advances in optics and photonics* **2011**, *3*, 161–204.

¹¹⁰Zhang, Y.; Zhao, H.; Wu, T.; Gao, Z.; Ge, L.; Feng, L. High-Dimensional Quantum Key Distribution by a Spin-Orbit Microlaser. *Phys. Rev. X* **2025**, *15*, 011024.

¹¹¹Whisler, C.; Holdman, G.; Yavuz, D. D.; Brar, V. W. Enhancing two-photon spontaneous emission in rare earths using graphene and graphene nanoribbons. *Phys. Rev. B* **2023**, *107*, 195420.

¹¹²Dodson, C. M.; Zia, R. Magnetic dipole and electric quadrupole transitions in the trivalent lanthanide series: Calculated emission rates and oscillator strengths. *Phys. Rev. B* **2012**, *86*, 125102.

¹¹³Safaei, A.; Chandra, S.; Vázquez-Guardado, A.; Calderon, J.; Franklin, D.; Tetard, L.; Zhai, L.; Leuenberger, M. N.; Chanda, D. Dynamically tunable extraordinary light absorption in monolayer graphene. *Physical Review B* **2017**, *96*, 165431.

¹¹⁴Paudel, H. P.; Safaei, A.; Leuenberger, M. N. In *Nanoplasmonics - Fundamentals and Applications*; Barbillon, G., Ed.; Intech: London, 2017; Chapter 3, p 1142.

¹¹⁵Safaei, A.; Chandra, S.; Shabbir, M. W.; Leuenberger, M. N.; Chanda, D. Dirac plasmon-assisted asymmetric hot carrier generation for room-temperature infrared detection. *Nature Communications* **2019**, *10*, 3498.

¹¹⁶Safaei, A.; Chandra, S.; Leuenberger, M. N.; Chanda, D. Wide Angle Dynamically Tunable Enhanced Infrared Absorption on Large-Area Nanopatterned Graphene. *Acs Nano* **2019**, *13*, 421–428.

¹¹⁷Shabbir, M. W.; Leuenberger, M. N. Theoretical Model of a Plasmonically Enhanced Tunable Spectrally Selective Infrared Photodetector Based on Intercalation-Doped Nanopatterned Multilayer Graphene. *ACS Nano* **2022**, *16*, 5529–5536.